

We are IntechOpen, the world's leading publisher of Open Access books Built by scientists, for scientists

6,900

Open access books available

185,000

International authors and editors

200M

Downloads

Our authors are among the

154

Countries delivered to

TOP 1%

most cited scientists

12.2%

Contributors from top 500 universities



WEB OF SCIENCE™

Selection of our books indexed in the Book Citation Index
in Web of Science™ Core Collection (BKCI)

Interested in publishing with us?
Contact book.department@intechopen.com

Numbers displayed above are based on latest data collected.
For more information visit www.intechopen.com



New Energy Harvesting Systems Based on New Materials

Lucian Pîslaru-Dănescu and
Lipan Laurențiu Constantin

Additional information is available at the end of the chapter

<http://dx.doi.org/10.5772/intechopen.72613>

Abstract

This study starts with the ZnO nanostructured materials used for improve the efficiency of polycrystalline solar cells operation under low solar radiation conditions. The ZnO nanowires were prepared using the hydrothermal method of deposition on the seed layer by a new and complex process, with controllable morphological and optical properties. The analysis of the XRD patterns, scanning electron microscopy images (SEM) of the ZnO nanowires and a lot of tests made Pasan Meyer Burger HighLight 3 solar simulator, confirm the advantages of using the ZnO nanowires in solar cells applications for antireflection coatings. Then, piezoelectric structures based on new modified PZT zirconate titanate designed for energy harvesting applications is presented. Based on their piezoelectric characteristics, modified PZT zirconate titanate ceramics made of Pb ($\text{Zr}_{0.53}\text{Ti}_{0.47}$) $_{0.99}\text{Nb}_{0.01}\text{O}_3$ ceramic have efficient applications in energy harvesting devices. A piezoelectric transducer, consisting of a thin plate of this piezoceramic material, with dimensions (34 mm × 14 mm × 1 mm), is illustrated. A multiphysics numerical simulation further illustrates such piezoelectric transducer operation. Finally, the miniature planar transformer with circular spiral winding and hybrid core—ferrite and magnetic nanofluid, designed for new energy harvesting systems is presented. We purpose now that the magnetic nanofluid be used both as a coolant and as part of the hybrid magnetic core.

Keywords: ZnO nanostructured materials, antireflection coatings, piezoelectric devices, energy harvesting, electric micro-transformer, planar coils, magnetic nanofluid

1. Using the ZnO nanostructured materials in order to improve the efficiency of polycrystalline solar cells operation under low solar radiation conditions

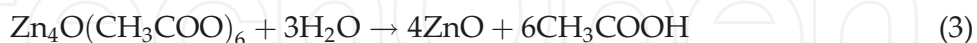
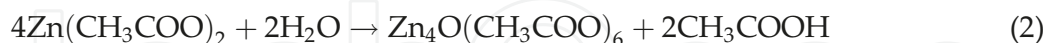
1.1. Current state regarding obtaining of the ZnO nanoparticles

ZnO is a II–VI semiconductor with direct band band of 3.37 eV. Nanostructured ZnO is used to obtain LED's (light-emitting diode – electroluminescent diode), in the manufacture of gas sensors and photovoltaic cells, both because of its electron transport properties and anti-reflective coatings. In recent years, a number of articles have been reported to present the results obtained from studies to obtain ZnO nanoparticles. The use of the hydrothermal method for obtaining these nanostructures using water as solvent and the $\text{Zn}(\text{NO}_3)_2$ – HMTA system, at low temperatures (below 100°C), is among the processes that have begun to be used in recent years. ZnO nanoparticles are relatively easy to synthesize due to the hexagonal columnar structure of the unit cell. Once with getting the nanobelts of ZnO in 2001 [1], the research of ZnO nanostructures with different morphologies has seen rapid growth. The different methods of synthesizing these nanoparticles have been developed in recent years; they include vapor–liquid–solid techniques [2, 3], chemical vapor deposition [4], thermal evaporation [5] and hydrothermal method [6, 7]. The hydrothermal method does not involve the use of catalysts and facilitates the growth of nanoparticles on large surfaces. The increase in the gaseous phase can be achieved using one of the following methods: chemical deposition of metal–organic vapors (MOCVD) [8, 9], chemical transport from vapor [10, 11] and deposition by laser ablation [12]. With these methods, high-quality nanoparticles of micron size [13, 14] can be obtained. The process presents a number of disadvantages: it requires a temperature of 450 – 900°C , a series of limitations related to the substrate are imposed like morphology and its area [15]. In contrast, growth from the solution is a process that takes place at temperatures below 100°C , [16, 17], and the advantage of this process is to obtain nanoparticles with optical and electrical properties necessary for their use in the field of photovoltaic cells (antireflection coatings, electrode transparent, etc.).

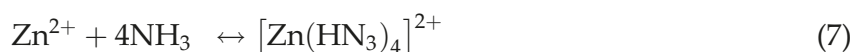
1.2. Preparation of antireflective coating based on ZnO nanoparticles for application on the substrate

Anti-reflection technology plays an important role in the fabrication of high-efficiency solar cells by increasing light coupling into the active region of devices. A complex process is used for obtaining ZnO nanostructures for antireflective coatings. The process is suitable to silicone solar cells and can be used in order to increase their efficiency under low solar radiation, allowing the control of the morphological and optical properties of ZnO nanostructures deposited on glass through ZnO seed layer deposition process. The ZnO nanowires were prepared using the hydrothermal method of deposition on the seed layer by a new and complex process, [18]. To obtain the ZnO nanoparticles, two steps are required: obtaining the ZnO seed layer (on which ZnO nanoparticles are formed) and a second stage consisting of the actual growth of ZnO nanoparticles. ZnO seeded layers were prepared using a solution of zinc acetate dissolved in 1-propanol. Zinc decomposition or hydrolysis to obtain ZnO nanocrystals are a method often used [19–21]. Subsequent decomposition of zinc acetate at temperatures between 100°C – 280°C leads to the formation of $\text{Zn}_4\text{O}(\text{CH}_3\text{CO}_2)_6$, which eventually breaks

down into ZnO. During the process of obtaining a ZnO by this method a series of gaseous products are released: water (H₂O), carbon dioxide (CO₂), acetone ((CH₃)₂CO) and acetic acid (CH₃COOH). These products are eliminated around the temperature of 270°C ((1)–(4)). As the temperature increases, ZnO nanoparticles are formed following chemical reactions:



Thus, thermal dehydration of zinc acetate can be considered a process of dehydration, vaporization/decomposition and ZnO formation [22]. Synthesis of ZnO nanowires by the hydrothermal method on the deposited substrate by the dehydrated zinc acetate process, involves the reactions:



HMTA hydrolyzes readily in water to form formic aldehyde (HCHO) and ammonia (NH₃), releasing energy, which is associated with its molecular structure, as can be seen in reactions (5) and (7). This stage is critical in the process of increasing ZnO nanowires. If HMTA hydrolyses very quickly, it produces a very large amount of OH[−] ions—in a very short time, Zn²⁺ ions from the solution would precipitate quickly due to the basic pH, and this would lead to rapid consumption of precursors and to an inhibition of the growth of ZnO nanoparticles [23]. From reactions (8) and (9), NH₃ which originates from hydrolysis HMTA has two essential roles. Firstly it produces the basic medium required for the formation of Zn(OH)₂. Secondly, it coordinates the Zn²⁺ ions and thus stabilizes the aqueous solution. Zn(OH)₂ is dehydrated when heated by ultrasonication or even under the sunlight. All five reactions (5), (6), (7), (8) and (9) are in equilibrium and can be controlled by adjusting the reaction parameters: precursor concentration, temperature and growth time, which may have a positive or negative influence on the balance of reactions. Thus, precursor concentration determines the nanoparticle density, temperature and growth time controls. It also controls the morphology and nanoparticle size ratio. In reaction (5) it can be seen that seven moles of reactants produce ten moles of reaction products, which means an increase in entropy during the reaction, resulting an increase of the temperature, and finally the result is the shift of equilibrium to the reaction products. The rate of hydrolysis of HMTA increases with the increase of the basicity of the environment and vice versa. Also, the five reactions continue at room temperature but at a very low speed. For example, the solution with a precursor concentration of less than 10 mmol/L remains transparent and clear at room temperature for several months. If microwaves are used

as a source of heating, the reactions take place at a very high speed, with a nanofire growth rate of up to 100 nm/min [24].

1.3. The analysis of ZnO seed layer and ZnO nanowires growth by the hydrothermal method

The X-ray diffraction analysis was performed for the ZnO seed layer as well as for the ZnO nanowires growth by the hydrothermal method as shown within **Figures 1** and **2** respectively. The structural analysis of the ZnO nanoparticles was performed, by grazing incident X-ray diffraction using an X-ray diffractometer (Bruker AXS D8 Discover) with Cu and $K\alpha$ irradiation, 40 kV/40 mA, 20–60°, 2 Theta domain, 2 seconds/step scan speed and 0.04° step. In the case of the ZnO seed layer, there were identified only the specific peaks of ZnO, confirming the higher purity of the film. ZnO from seed layer presented *wurtzite* hexagonal structure $P63mc$ as well as structure parameters $a = b = 3.242$ nm and $c = 5.176$ nm. The intensity of the diffraction peaks corresponding to (002) and (110) plans displayed low broad peaks in the case of all the analyzed seed layer samples. The XRD analysis showed wurtzite hexagonal structure $P63mc$ and structure parameters $a = b = 3.242$ nm and $c = 5.176$ nm when also considering the nanowires. The diffraction pattern highlighted peaks associated to (100), (002), (101) and (102) plans and the correspondence of ZnO. The (002) plan displayed a higher intensity peak in comparison to the corresponding plans (100), (101) and (102), indicating that the ZnO nanowires are predominantly c-axis orientated. Other peaks were not observed, leading to the fact that no other structures besides ZnO were formed. It was confirmed that high purity ZnO is obtained.

A different number of depositions (spray pyrolysis and spin coating) were achieved in order to determine the optimal thickness and morphology of the ZnO seed layer. The optimal seed

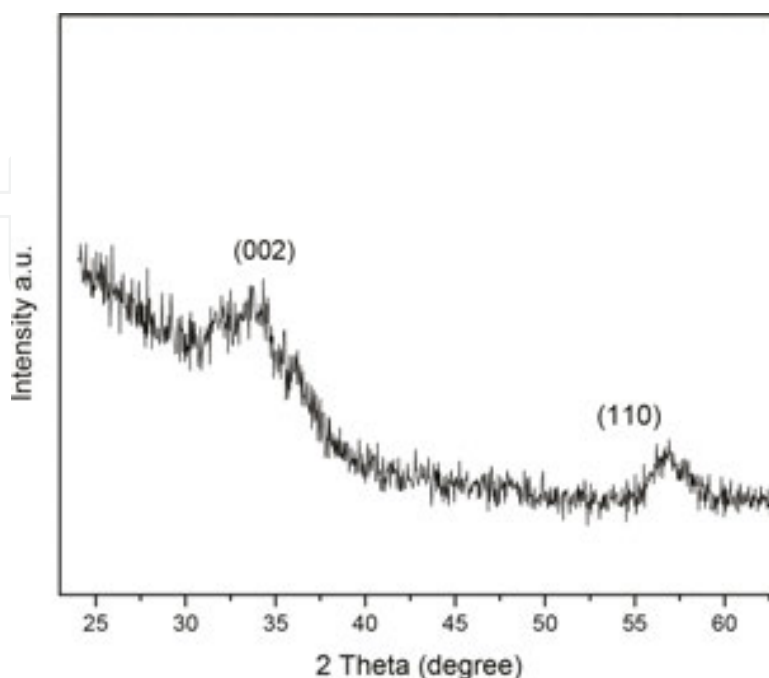


Figure 1. XRD analysis of ZnO seed layer.

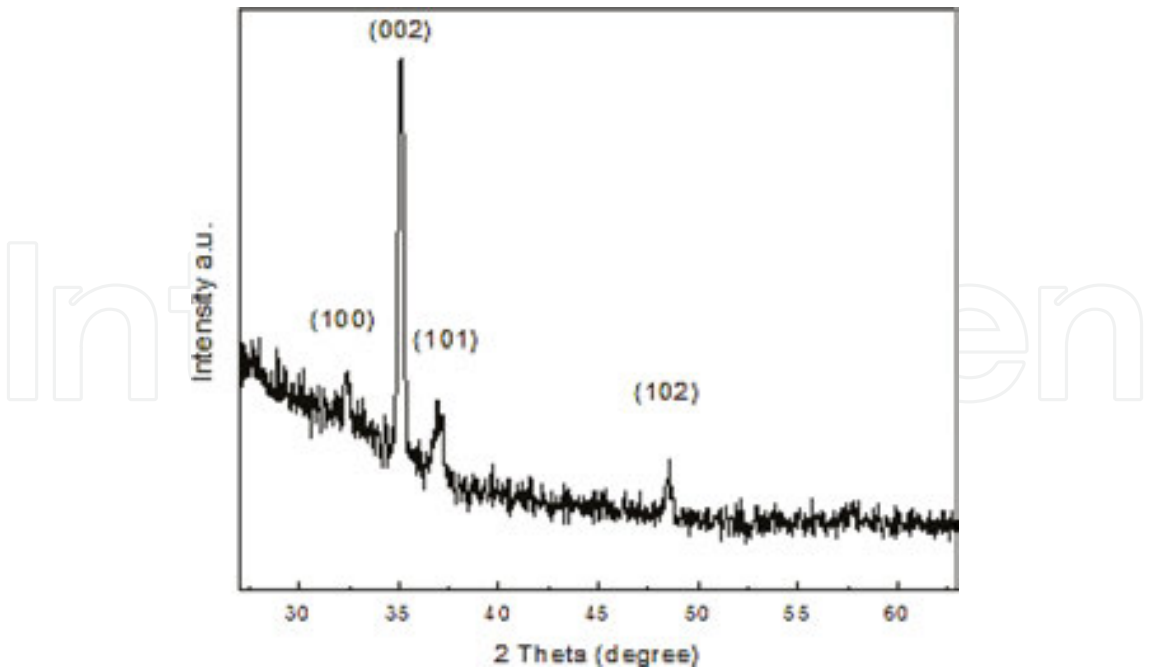


Figure 2. XRD analysis of ZnO nanowires growth by the hydrothermal method [18].

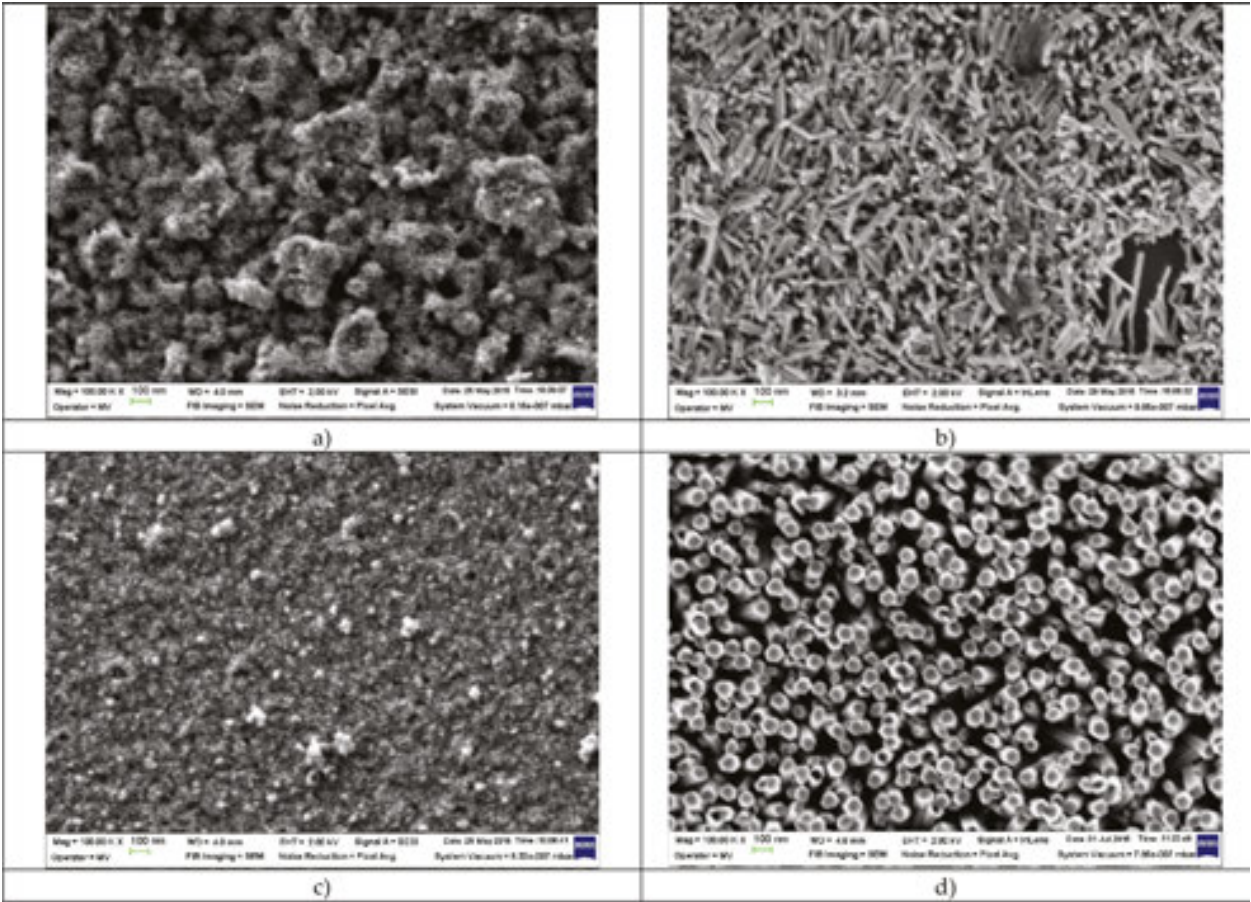


Figure 3. Scanning electron microscopy (SEM) images of the ZnO seed layer (a) and (c) as well as SEM images of ZnO nanowires (b) and (d) respectively [18] (100 kx magnification).

layer was obtained by three application stages of spray pyrolysis at a temperature of 100°C, three stages of spin coating followed by treatment at 300°C for a period of 30 minutes.

The microscopy micrographs shown within **Figure 3** were recorded by using a field scanning electron microscope or by employing the annular in-lens detector for a second set of electron images with magnification of 100.000 X and an accelerating voltage of 2000 V. The surface morphology and structure of the nanoparticles were examined by employing a scanning electron microscope (FESEM, Carl Zeiss Auriga) at an accelerating voltage of 2.00 kV. The imaging was performed at a high magnification of 100 kx while the optical transmission and reflection spectra was recorded in the wavelength range of 400–800 nm by using a double beam UV–Vis–NIR spectrophotometer (UV–VIS Spectrophotometer 570 Jasco). The morphology of the ZnO seed layer surface influences the morphology of the ZnO nanowire. These layers operate as seed crystals in order to ensure the epitaxial growth of ZnO nanowires. In the case of thicker films, ZnO clusters are observed (grains with dimensions larger than 100 nm) consisting of agglomerations that influence the nanowires growth by a reduced order, scattered across the surface and random orientated (**Figure 3a** and **b**). The morphology and growth of the zinc oxide nanowires are influenced by the thickness and geometry of the seed layer (uniform grain, 30–55 nm) (as seen from **Figure 3c** and **d**). In this case, due to the seed layer uniformity and lack of agglomerations, the nanowires growth was orientated, with homogenous dimensions as well as displayed on the entire substrate surface. In this case, there was obtained a perfectly balanced seed layer and also a homogenous nanowire growth with lengths of ~200 nm and 50 nm diameter. Besides the high density of the ZnO nanowire arrays, other nanostructures are not observed.

The resulting seed layer presented suitable growth proprieties by the hydrothermal method of uniform and vertical ZnO nanowires. The variation of the optical transmission is shown within **Figure 4**, with wavelength found in the range of $\lambda = 400\text{--}800$ nm for glass, ZnO seed layer and ZnO nanowires. The ZnO seed layer has presented a good transparency of approximately 80%, similar to the glass value due to the reduced thickness (50 nm) and surface uniformity. The

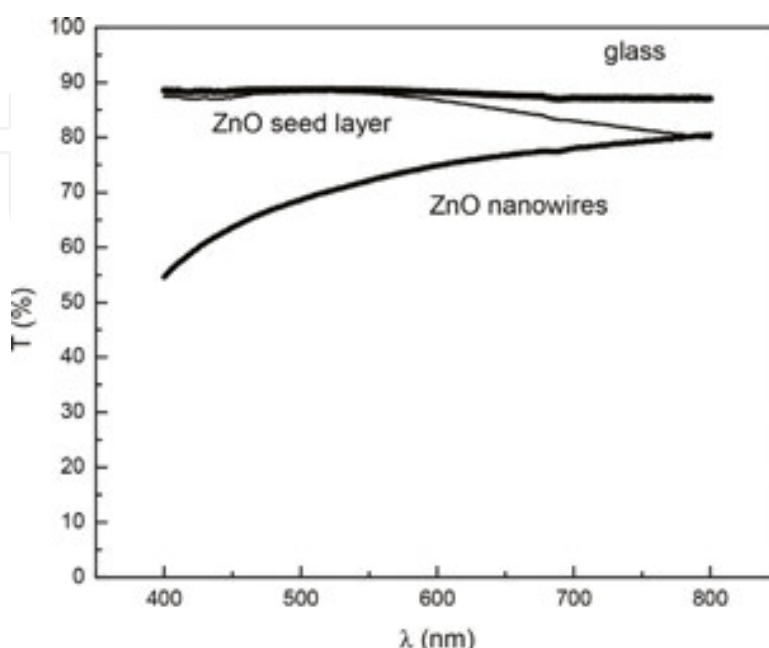


Figure 4. Optical transmission of glass, ZnO seed layer and ZnO nanowires film.

samples of ZnO nanowires present a good transparency in the visible range (400–800 nm), with a lower average value of 76% (approximately 5% lower than in the case of glass). This decrease is due to the fact that the transmitted radiation by light diffusion increases the occurrence of the light scattering phenomenon of the ZnO nanowires.

Following the spectrophotometric analysis, the variation of the optical reflection with wavelength in the range of 400–800 nm is presented in **Figure 5**. The graph confirms that the reflection is reduced in comparison to the values obtained for simple glass. The ZnO seed layer presents an intermediate value between glass and ZnO nanowires, with an average of 11%. The average value of ZnO nanowires sample for the visible optical reflection is equal to 9%, with 5% lower than the simple glass. By summarizing these optical characteristics, it is concluded that the ZnO nanowire films can be considered as a solution to the antireflective coatings in the solar cells field due to the optical proprieties and low-price manufacturing.

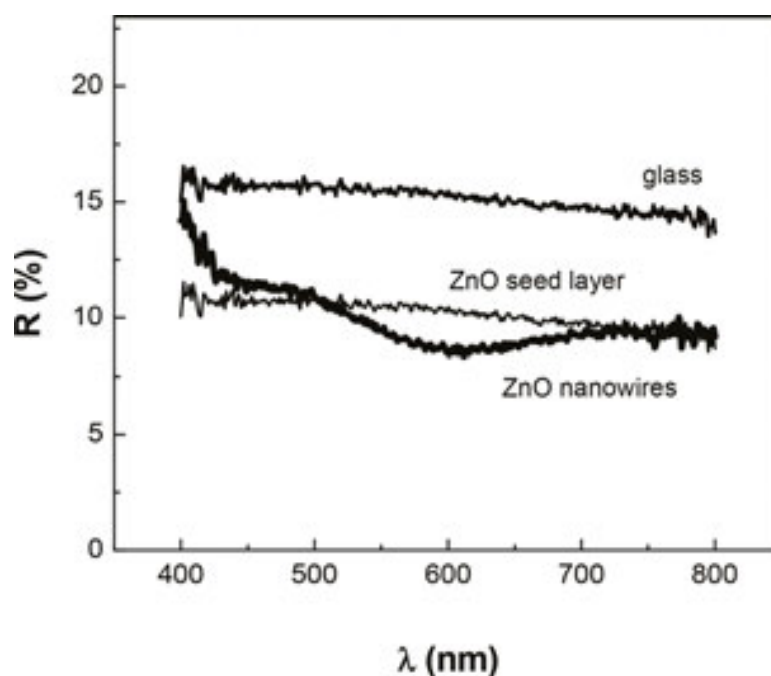


Figure 5. Optical reflection of glass, ZnO seed layer and ZnO nanowires film.

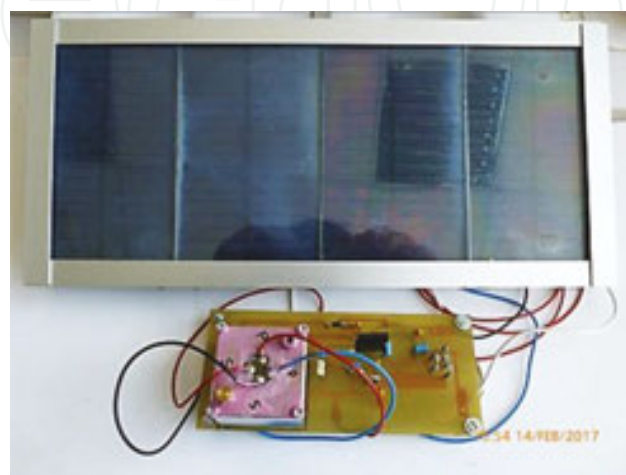


Figure 6. The modular photovoltaic conversion system, connected to the DC/DC converter with isolation.

1.4. Prototyping and testing the modular photovoltaic conversion system

Modular photovoltaic conversion system, designed for energy harvesting applications has been achieved, using four photovoltaic cells, **Figure 6**. A commercial polycrystalline silicone solar cell manufactured by Conrad Electronic SE was selected and covered by a nanostructured ZnO disposed on glass in order to be tested. The technical data related to the considered polycrystalline solar panel (123 cm²) consist of 1.35 W output power, 9 V nominal voltage, 10.5 V open circuit voltage and 150 mA short-circuit current. The determination of the solar

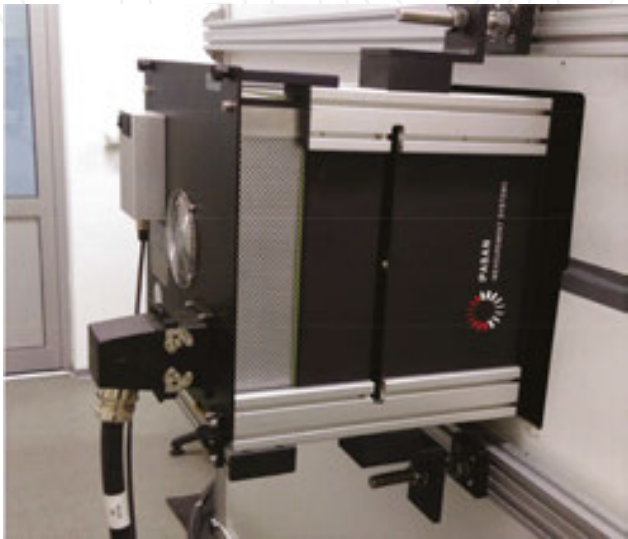


Figure 7. Pasan Meyer Burger HighLight 3 solar simulator, used to test of the modular photovoltaic conversion system, view from flash box.

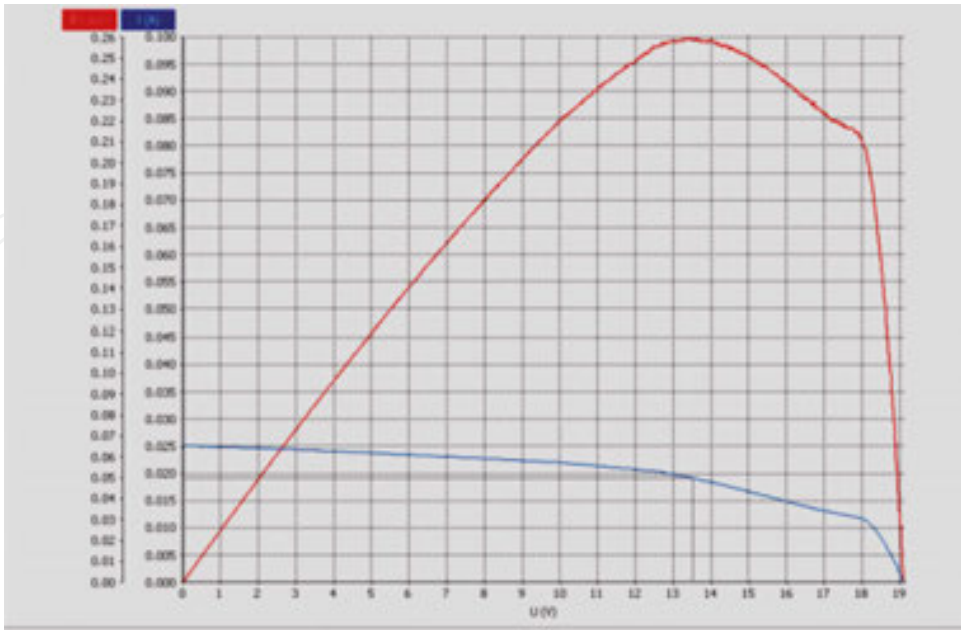


Figure 8. Tested of the photovoltaic module covered by a nanostructured ZnO disposed on glass, for 100 W/m² test conditions.

cells functional parameters (efficiency, short circuit current, open circuit voltage and output power) has led to the conclusion that all the values are superior in the case of the solar cells with ZnO nanowires on glass showing that the performance of the solar cell depends on the irradiance and antireflective coating.

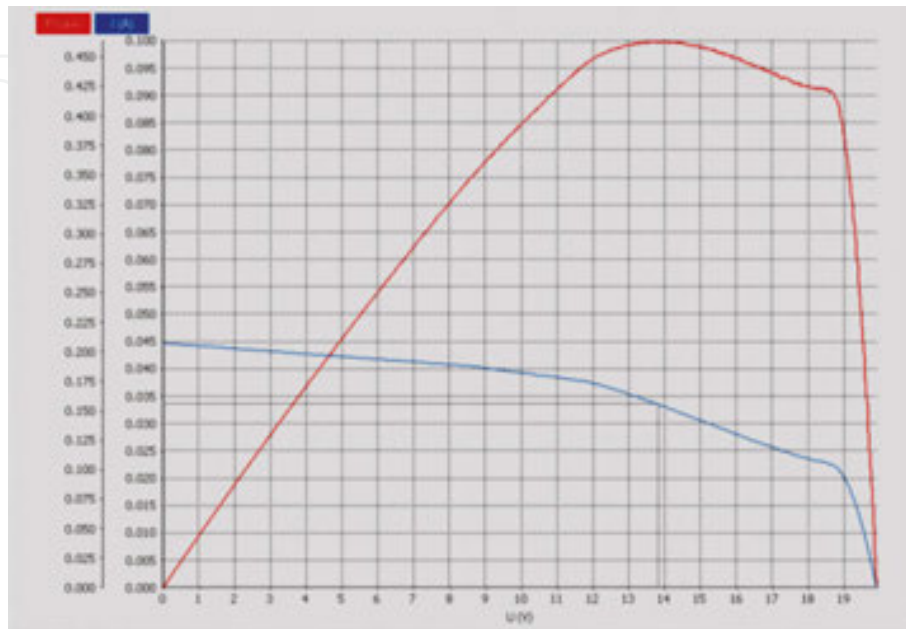


Figure 9. Tested of the photovoltaic module covered by a nanostructured ZnO disposed on glass, for 200 W/m² test conditions.

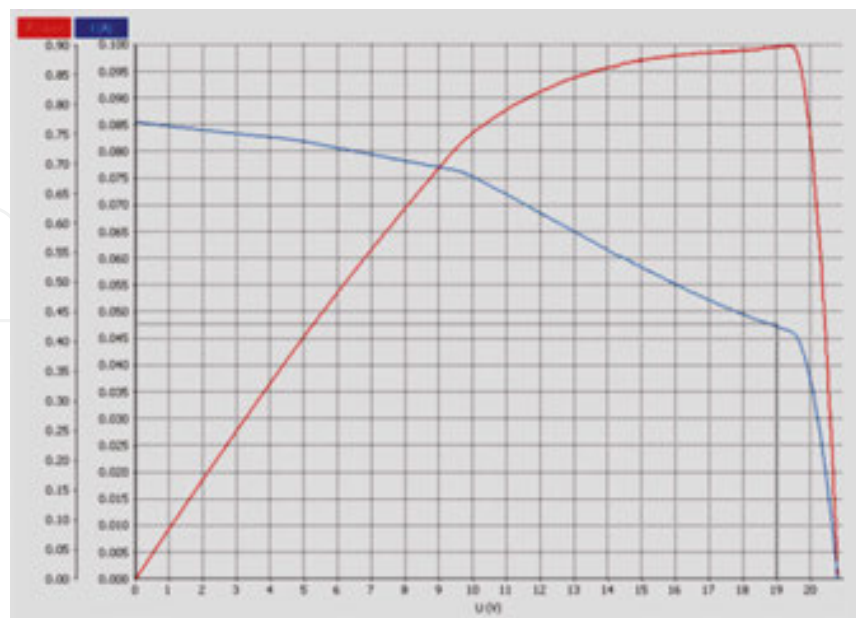


Figure 10. Tested of the photovoltaic module covered by a nanostructured ZnO disposed on glass, for 400 W/m² test conditions.

The photovoltaic module was tested for standard test conditions (1000 W/m^2 , 25°C , AM 1.5) as well as for reduced solar irradiance by using the Pasan Meyer Burger HighLight 3 solar simulator shown in **Figure 7**. There were used four masks for the solar irradiance attenuation (100 W/m^2 , 200 W/m^2 , 400 W/m^2 and 700 W/m^2) in order to achieve the comparison between the generated powers along with varying the operation conditions. The used simulator is able

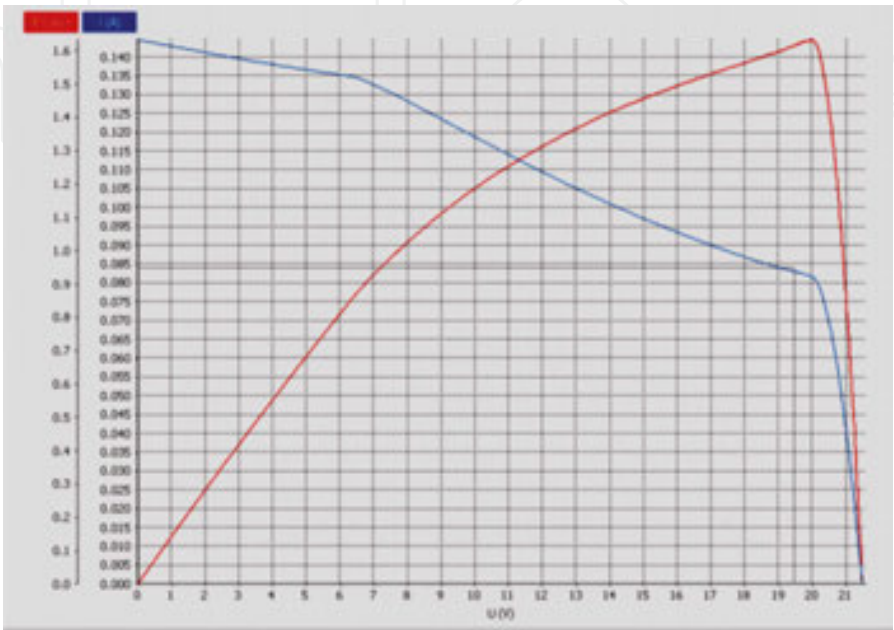


Figure 11. Tested of the photovoltaic module covered by a nanostructured ZnO disposed on glass, for 700 W/m^2 test conditions.

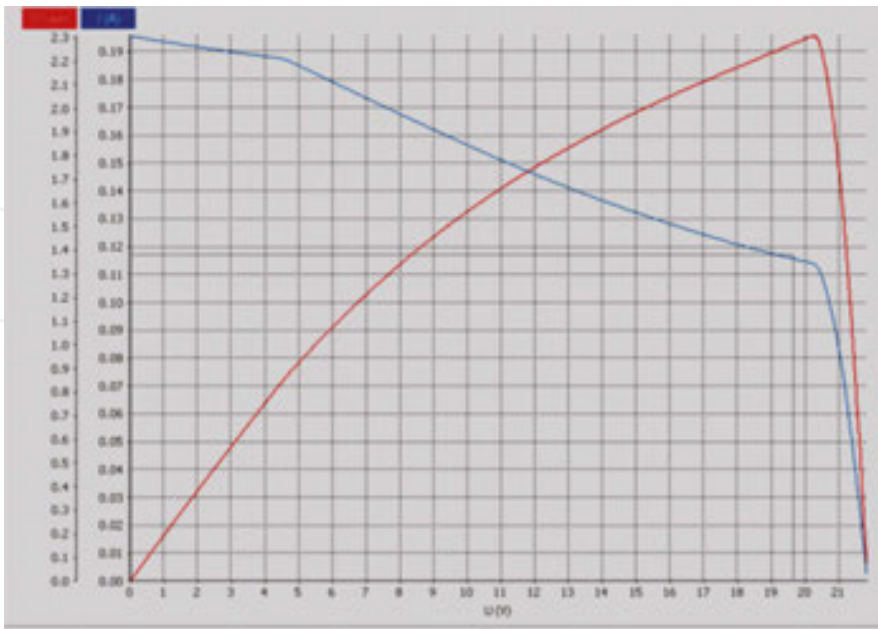


Figure 12. Tested of the photovoltaic module covered by a nanostructured ZnO disposed on glass, for standard test conditions, 1000 W/m^2 .

to adjust the irradiance value between 100 W/m^2 and 1000 W/m^2 , with both the light uniformity and light stability below 1%. Accordingly, five characteristics resulted for each of the tested modules for these various operating conditions, **Figures 8, 9, 10, 11 and 12.**

The results confirm the advantages of using the ZnO nanowires in solar cells applications for antireflection coatings.

2. Piezoelectric structures based on new modified PZT zirconate titanate designed for energy harvesting applications

We propose a piezoelectric ceramic material what can it be integrated into piezoelectric structures for energy harvesting applications. The piezoceramic element has the shape of a disk with diameter of 12 mm while the width is 0.3 mm. On each of the ceramic disk's sides, silver

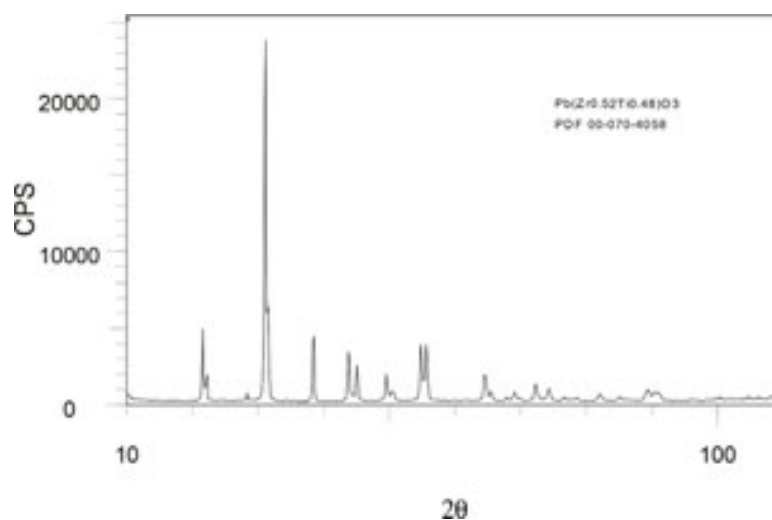


Figure 13. XRD pattern of PZT doped with 1% Nb_2O_5 sintered at 1120°C for 2 hours, [25].

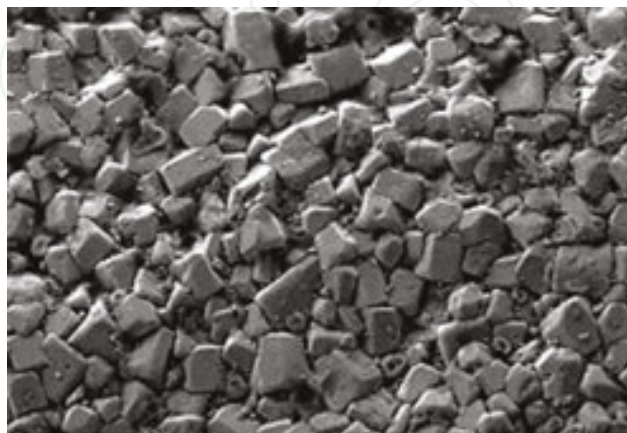


Figure 14. Scanning electron microscopy images (SEM) image of PZT doped with 1% Nb_2O_5 . Sintered at 1120°C for 2 hours [25].

electrodes were attached. Perovskite ceramics based on lead zirconate titanate (PZT) modified with niobium (Nb) were used to obtain these active elements. A high temperature solid state reactions technique has been used to prepare the piezoelectric ceramic, [25, 26], described by the general formula $\text{Pb}(\text{Zr}_{0.53}\text{Ti}_{0.47})_{0.99}\text{Nb}_{0.01}\text{O}_3$. Based on their piezoelectric characteristics, modified PZT zirconate titanate ceramics have efficient applications in energy harvesting devices. The X-ray diffraction patterns of $\text{Pb}(\text{Zr}_{0.53}\text{Ti}_{0.47})_{0.99}\text{Nb}_{0.01}\text{O}_3$ ceramic are shown in **Figure 13**. The XRD results indicate the rovskite type tetragonal phase free from a pyrochlore phase. The SEM pattern of the same composition sample is shown in **Figure 14** and it shows that the microstructure of our sample is very dense.



Figure 15. The low energy source built with piezoelectric linear transducers system, INC DIE ICPE-CA concept [26].

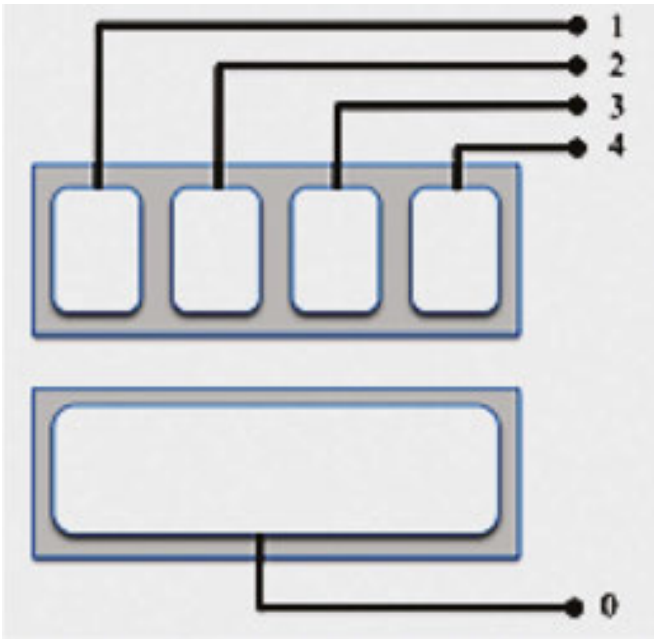


Figure 16. The electrical circuit of the generator [26].

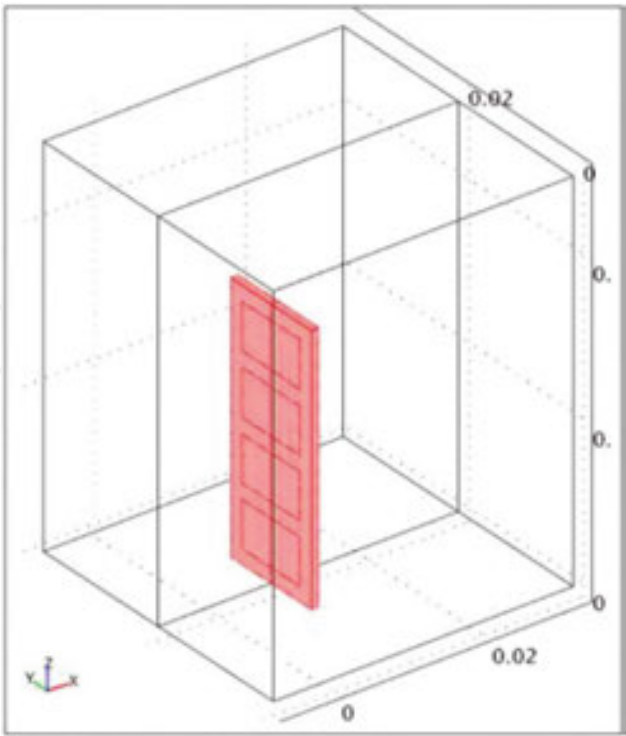


Figure 17. Computational domain for the flow problem (the plate is placed in a flow duct, as in a hydrodynamic test setting) (concept ECEE-UPB) [26].

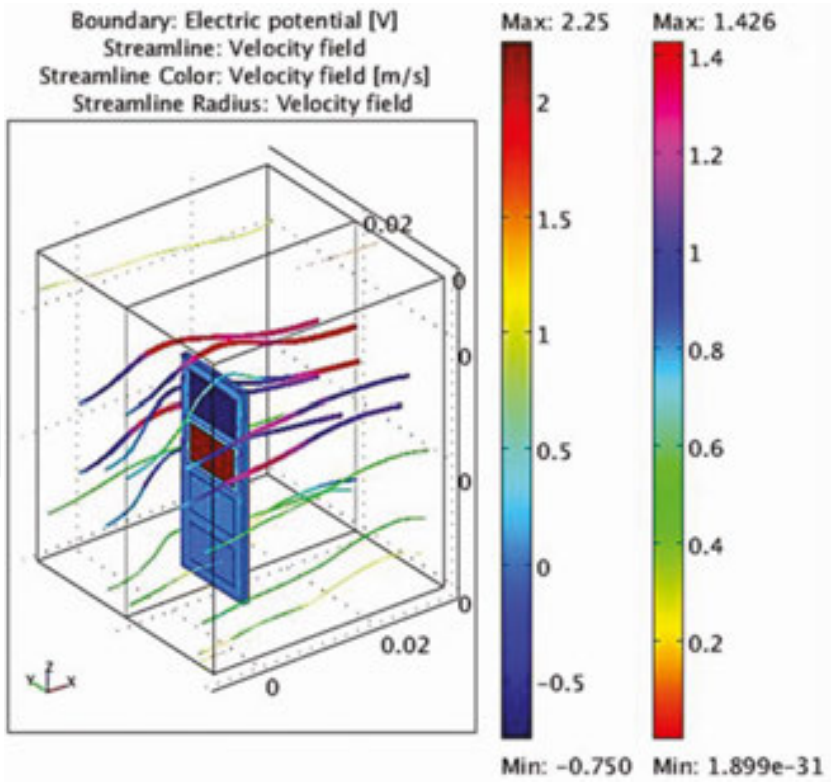


Figure 18. Solutions of the multiphysics problem: Fluid streamlines and electric potential color map on the surface of the plate (concept ECEE-UPB) [26].

A simple structure is analyzed in [25], by numerical simulation for the demonstration of its capacity to generate electric voltage under mechanical stress.

Another piezoelectric transducer, consisting of a thin plate of piezoceramic material with dimensions (34 mm × 14 mm × 1 mm), is illustrated in **Figure 15**. A layer of conductive material is deposited on one side of the plate (see the lower picture in **Figure 15**) and four equal rectangular conductive areas are deposited on the other side (see the upper picture in **Figure 15**), [26]. If the plate is subjected to pressure and mechanical deformation, due to exposure to wind or being placed in a fluid flow, the piezoelectric material will be polarized and a non-uniform electrical potential distribution could be identified on the faces of the plate. Conductive surfaces behave like surface electrodes attached to the plate; they integrate the electric potential on the plate's surface and connect to an electric circuit, transferring the potential value of each plate to an output connector, **Figure 16**. The one face which is uniformly coated can be used for reference terminal (ground), while each of the four rectangular patches can be connected to an individual electrode (1, 2, 3, 4), **Figure 16**. If the deformation of the ceramic plate is not uniform (the case of a flexible material), the electrodes might take different potential values and the piezoceramic plate becomes an electrical generator with four different output voltages: U_{10} , U_{20} , U_{30} , U_{40} , **Figure 16**. If the plate is rigid and the deformations are identical, the four terminals provide equal output voltages, [26].

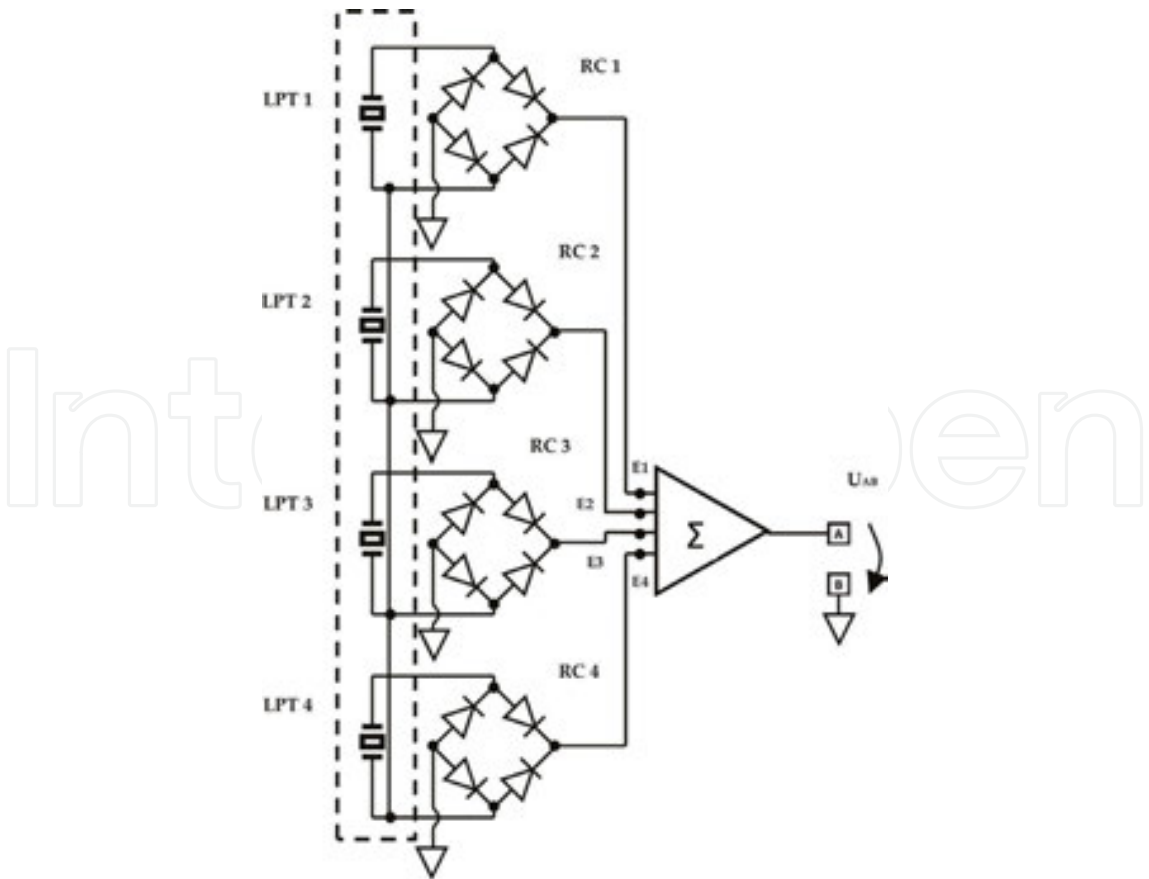


Figure 19. Interfacing of the low energy source built with piezoelectric linear transducers system [26].

A multiphysics numerical simulation further illustrates such piezoelectric transducer operation. The numerical model was built and analyzed with Comsol Multiphysics [38], a technical software package based on the finite element method, which allows the coupling of different software modules specialized in modeling physical problems of different nature. An image of the solution of this analysis is presented in **Figures 17 and 18**.

Often, due to the complexity of the mathematical model, the analytical solutions of the differential equations system are difficult to be obtained. Thus, it is necessary to use the numerical simulations method still from the design phase.

Interfacing of the low energy source built with piezoelectric linear transducers system is achieved through four bridges, as shown in **Figure 19**.

3. Miniature planar transformer with circular spiral winding and hybrid core—ferrite and magnetic nanofluid designed for new energy harvesting systems

One of the novelties of the future harvesting devices is regarding the use of a magnetic liquid core micro-transformer for the DC-DC converter of the harvesting device. From the operating point of view, by replacing the solid core with a hybrid core—ferrite and magnetic nanofluid, we estimate to result in a better heat dissipation and a reduction the thermal stresses in the micro-transformer leading to a longer life cycle of the device, maintaining or even improving the electric characteristics. Also, the dielectric properties of the micro-transformer will be improved.

3.1. Making a planar microtransformer with circular spiral windings with hybrid core—ferrite and colloidal magnetic nanofluid: V1 by using LIGA technology (Litographie, Galvanoformung, Abformung) and precision micromachining

Energy harvesting is a relatively new research area, seen as a viable and affordable solution for powering small autonomous devices, such as wireless sensor networks. Energy harvesting devices use small scale parts with low power losses. The main components are the electrical transformers that convert the voltage/current parameters from the primary from the energy harvesting stage, to the secondary to energy storage and distribution level stage. Miniature construction of the transformers, whose implementation can benefit from the LIGA manufacturing technology (Litographie, Galvanoformung, Abformung or in English Lithography, Electroplating and Molding), are required for compact, small but energy-efficient solutions. The following steps are performed to manufacture a planar microtransformer with circular spiral windings and with hybrid core—ferrite and colloidal magnetic nanofluid—V1:

A. Manufacture of the planar micro-coils:

- the ceramic substrate preparation, 1, as well as surface preparation, (**Figure 20a**) and depositing conductive uniform submicrometer layer, 3;
- spin deposition (coat) of a uniform layer, 2, SU8 photoresist, (**Figure 20a**). The thickness of this layer will be slightly above the height of turns to be deposited;

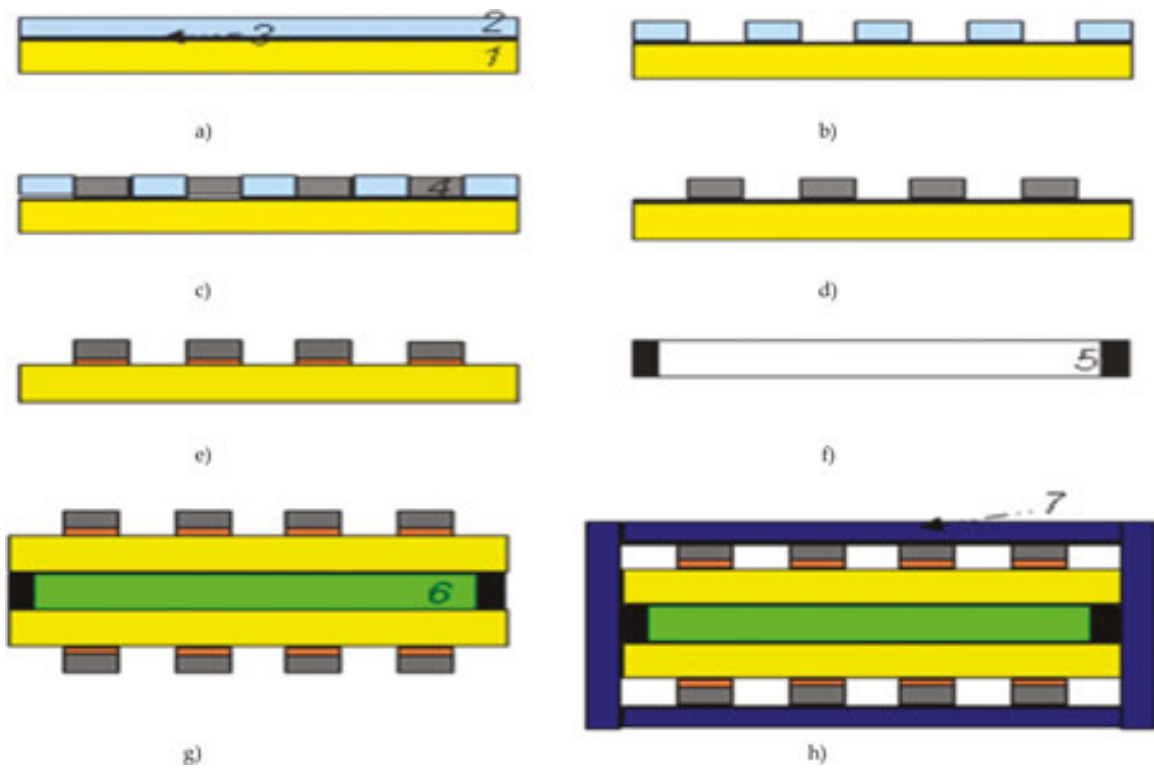


Figure 20. Manufacture of a planar microtransformer with circular spiral windings with hybrid core—ferrite and colloidal magnetic nanofluid—V1.

- pre-exposure bake (soft bake) at 95°C;
- exposure to UV radiation by direct writing lithography using DWL66 equipment;
- post-expose bake at 65°C and 95°C, with controlled ramp;
- relax and develop structures using 1-methoxy-2-propyl acetate (mr-DEV600), (**Figure 20b**);
- dry, hard bake;
- high purity copper galvanic deposition, 4, with controlled thickness (**Figure 20c**);
- SU8 photoresist exposed remove using free radical reaction with STP2020/R3T equipment (**Figure 20d**);
- controlled corrosion (remove) submicrometer layer to separate planar microcoils (**Figure 20e**);
- integrity coils checking.

B. *Manufacture of another parts:*

- precision micromachining by CNC machine (KERN Micro) by laser ablation CompexPro/Coherent and by electrodischarge machine on SmartDEM/Kunth: separation and sealing element, 5, (**Figure 20f**) and ferrite clad, 7, (**Figure 20h**).

C. The assembling:

- aligning the plates with micro-coils (two) by means of the separation and seal element, 5, (**Figure 20g**);
- undismantled adhesion assembly (bonding);
- introducing a magnetic nanofluid, 6, (**Figure 20g**), in the cavity and sealing the nozzle access;
- mounting plate ferrite isolated from coils and making of electrical connections.

3.2. Making a miniature planar microtransformer with circular spiral windings obtained by machining, starting from a textolit board double plated with copper and with hybrid core—ferrite and colloidal magnetic nanofluid

3.2.1. Making a miniature planar microtransformers with circular spiral windings with hybrid core—ferrite and colloidal magnetic nanofluid: V2

A key component of the devices used for energy harvesting from the environment is the electric transformer. In this case, we proposed a miniature planar transformer with circular spiral windings with hybrid core—ferrite and colloidal magnetic nanofluid, [27]. The proposed model has two circular spiral-wound, made from copper: 20 turns in primary and 40 turns in secondary. Windings, **Figures 21** and **22**, can be “grown” using LIGA technology on a ceramic substrate (Al_2O_3) as has been shown previously or can be obtained by machining, starting from a textolit board double plated with copper. Housing and central column are made of 3F3 ferrite. The cavity formed in the housing is filled with superparamagnetic colloidal nanofluid, NMF-UTR40-500G, **Figure 21**, having saturation magnetization of 500 Gs, [27]. The applications presented in [28, 29], uses a dilution of magnetic nanofluid acting also as a cooling agent, type NMF-UTR40-50G that having saturation magnetization of 50 Gs.

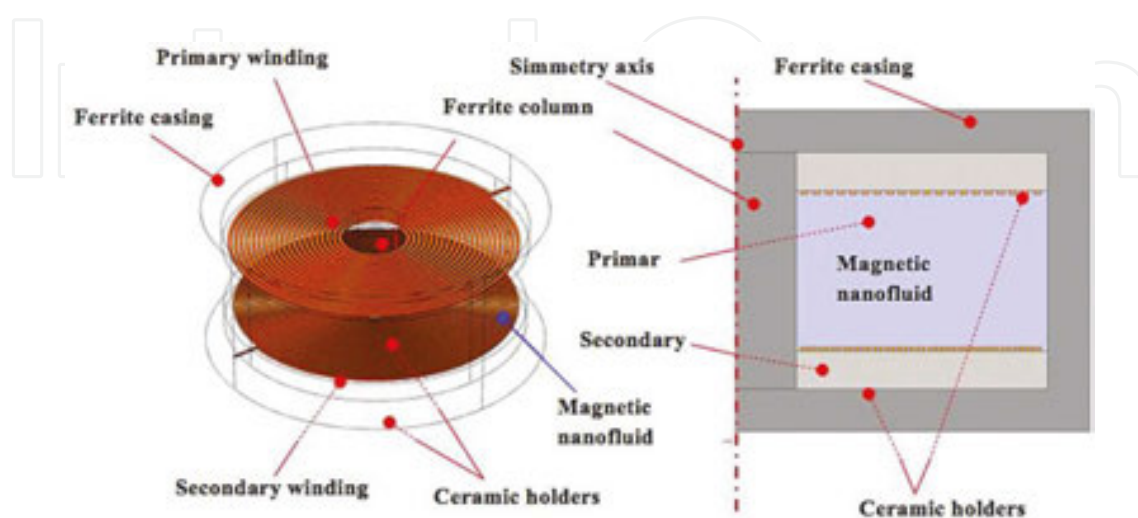


Figure 21. The planar microtransformers with circular spiral windings with hybrid core—ferrite and colloidal magnetic nanofluid—V2 and the equivalent simplified 2D axial model [30].



Figure 22. Planar coils corresponding to primary and secondary coils of the microtransformer, INCDIE ICPE-CA concept.

We purpose now that the magnetic nanofluid be used both as a coolant and as part of the hybrid magnetic core, by using of the magnetic nanofluid type NMF-UTR40-500G.

3.2.1.1. The mathematical model

The magnetic field inside the planar microtransformers with circular spiral windings with hybrid core—ferrite and colloidal magnetic nanofluid—V2 for steady state conditions is described by the (10), (11), (12) and (13) equations as follows: inside the coils ($\mathbf{J} \neq 0$), the ferrite part of the magnetic core ($\mathbf{J} = 0$), and within the ceramic holders ($\mathbf{J} = 0$).

$$\nabla \times (\mu_0^{-1} \mu_r^{-1} \nabla \times \mathbf{A}) = \mathbf{J}, \quad (10)$$

inside the magnetic nanofluid (MNF) core.

$$\nabla \times (\mu_0^{-1} \nabla \times \mathbf{A} - \mathbf{M}) = 0, \quad (11)$$

where \mathbf{A} [T.m] is the magnetic vector potential, \mathbf{J} [A/m²] is the electric current density, $\mu_0 = 4\pi \times 10^{-7}$ H/m is the magnetic permeability of the free space, μ_r is the relative magnetic permeability, and \mathbf{M} [A/m] is the magnetization of the MNF, approximated here through, $\mathbf{M} = \alpha \arctan(\beta \mathbf{H})$, where \mathbf{H} [A/m] is the magnetic field strength, and α, β are empiric constants selected to accurately fit the magnetization curve. The problem is closed by magnetic insulation boundary conditions, $\mathbf{n} \times \mathbf{A} = 0$, where \mathbf{n} is the outward pointing normal, [30–32].

The magnetic field, produced by the electric currents, generates magnetic body forces within the MNF, which are responsible for the flow of the fluid part of the core described, in steady state conditions, through.

momentum conservation (Navier–Stokes)

$$\rho(\mathbf{u} \cdot \nabla) \mathbf{u} = -\nabla \times [p\mathbf{I} + \eta \nabla \mathbf{u} + (\nabla \mathbf{u})^T] + \mathbf{f}_{mg}, \quad (12)$$

mass conservation law

$$\nabla \cdot \mathbf{u} = 0, \quad (13)$$

where, \mathbf{u} [m/s²] is the velocity, p [N/m²] is the pressure, ρ [kg/m³] is the mass density, η [N·s/m²] is the dynamic viscosity, and $\mathbf{f}_{mg} = \mu(\mathbf{M} \cdot \nabla)\mathbf{H}$ [N/m³] is the magnetization body force. Body forces of thermal nature are not significant here [30–32]. No slip (zero velocity) conditions on the outer boundaries of the MNF core close the flow problem.

3.2.1.2. The practical achievements

In **Figure 23**, the 3F3 ferrite parts of magnetic circuit can be seen and in **Figure 24** the ferrite magnetic circuit and microtransformer housing. Parts of the housing, the ferrite magnetic circuit and the four planar coils which form the primary and the secondary circuit of the microtransformer it can be seen in **Figure 25**. Finally, two assembled planar microtransformers are represented in **Figure 26**.



Figure 23. The 3F3 ferrite parts of magnetic circuit.



Figure 24. The ferrite magnetic circuit and microtransformer housing.



Figure 25. Parts of the housing, the ferrite magnetic circuit and the four planar coils which form the primary and the secondary circuit of the microtransformer, INCDIE ICPE-CA concept [33].

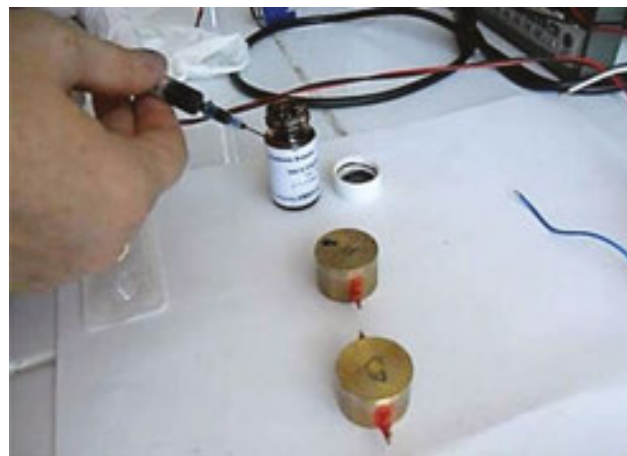


Figure 26. Two assembled planar microtransformers with circular spiral windings with hybrid core—ferrite and colloidal magnetic nanofluid—V2, after the magnetic nanofluid loading process.

3.2.1.3. Analysis of 3F3 ferrite as part of magnetic circuit

Analysis of 3F3 ferrite done by scanning electron microscopy (SEM) coupled with energy dispersive micro-probe X-ray under the following conditions:

The two areas of interest were at an increase of $5000\times$ and $2000\times$, **Figures 27 and 29**;

- Acquisitions have been made with the help of the secondary electron detector in the sample chamber, type “Everhart – Thornley”, coupled with “INCA Energy 250” energy dispersive microprobe produced by Oxford Instruments;
- Two categories of spectra were achieved, namely: punctual, with the elemental distribution of the electron beam spot on the surface of the sample and another as micro-area, integrated where the composition of the elements of the microarray was determined quantitatively;

- Spectral analysis is multipoint type because the spectra were superimposed to see the intensity and variation of the elements in the selected points/areas;
- All the spectra were normalized to 100%. The unit was expressed in the concentration of the elements of interest was the percentage by mass (weight percent%).

After analysis, the following features were noted:

- Elements that were highlighted were C, O, Mn, Fe and Zn, **Tables 1 and 2** and **Figure 28** for Spectrum 1;

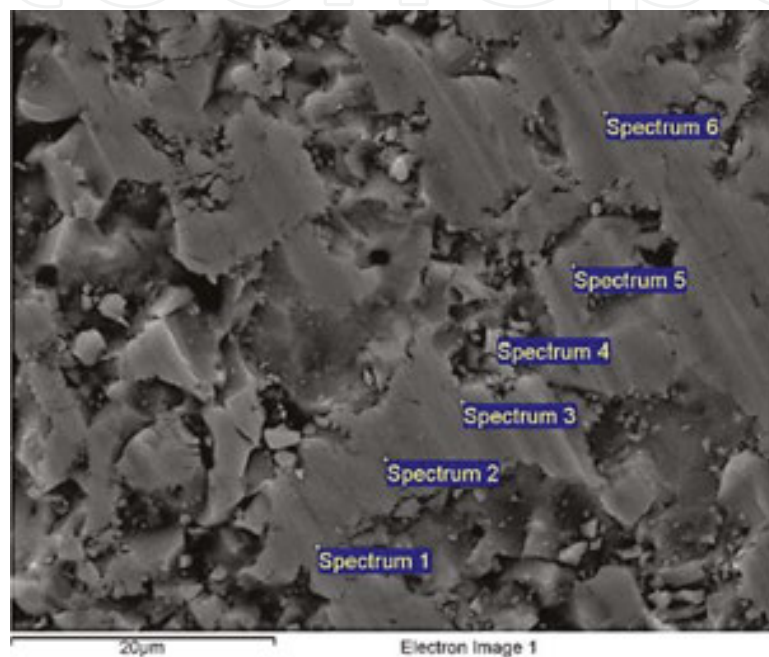


Figure 27. Scanning electron microscopy image (SEM) of the 3F3 ferrite, 5000× magnification.

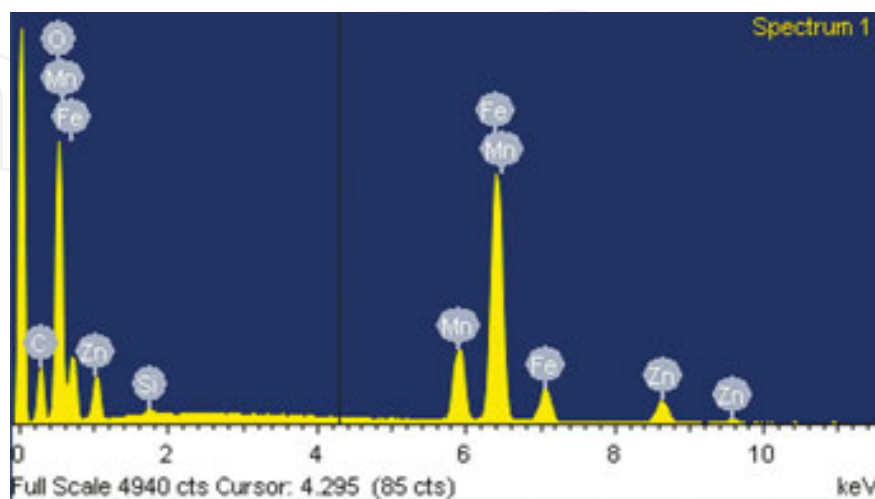


Figure 28. The 3F3 spectra analyze, corresponding to Spectrum 1 and 5000× magnification.

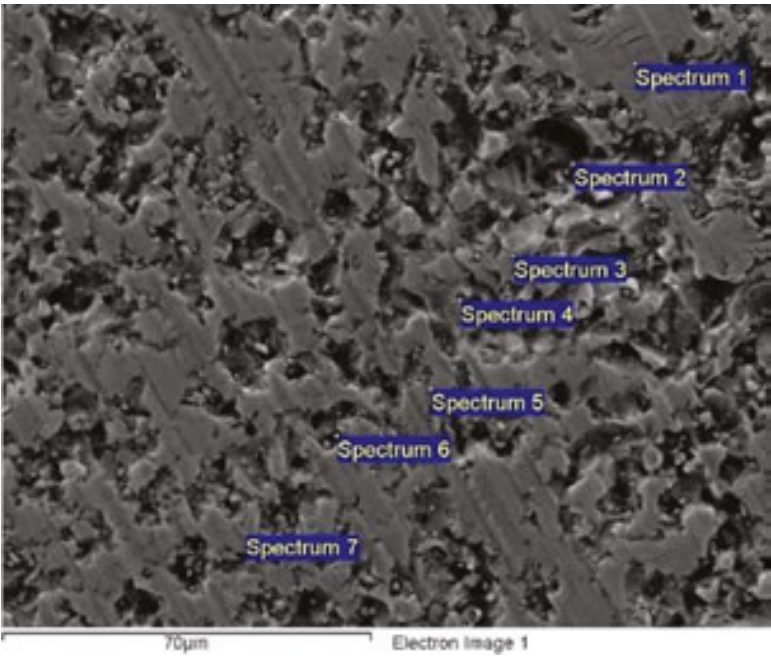


Figure 29. Scanning electron microscopy image (SEM) of the 3F3 ferrite, 2000× magnification.

Processing option: all elements analysed (normalised); all results in weight%							
Spectrum	In stats.	C	O	Mn	Fe	Zn	Total %
Spectrum 1	Yes	25.46	22.63	9.14	35.20	7.57	100.00
Spectrum 2	Yes	21.64	27.47	8.73	35.16	7.00	100.00
Spectrum 3	Yes	12.80	24.98	10.93	42.17	9.13	100.00
Spectrum 4	Yes	19.72	28.91	8.77	34.95	7.65	100.00
Spectrum 5	Yes	16.97	26.78	9.80	37.90	8.55	100.00
Spectrum 6	Yes	15.95	27.84	9.71	38.17	8.33	100.00
Mean		18.76	26.44	9.51	37.26	8.04	100.00
Std. deviation		4.49	2.28	0.83	2.80	0.77	
Max.		25.46	28.91	10.93	42.17	9.13	
Min.		12.80	22.63	8.73	34.95	7.00	

Table 1. Normalized values of elements obtained from spectral analysis of ferrite 3F3, corresponding to Spectrum 1–6, 5000× magnification.

- The presence of oxygen in percent more than 20% indicates that the sample contains oxides with various chemical combinations. The compositional distribution of the highlighted elements is relatively uniform, variations being probably due to the surface geometry of the sample (roughness of hundreds of nm) or to a non-uniform distribution of the carbon matrix (**Figure 29**);
- SEM micrographs have revealed a relatively uniform surface in terms of morphology, but which has a roughness due to the technological methods of obtaining the samples (of the

intrinsic material) or the mechanical processing methods used to obtain the investigated piece;

- It is also observed the presence of some impurities on the surface of investigated samples such as Al, Si and Ca elements, **Table 2** and **Figure 30** for Spectrum 1, but in very small percentages and they are not likely to jeopardize their functional role.

3.2.1.4. Magnetic nanofluids used for planar microtransformers with circular spiral windings with hybrid core—ferrite and colloidal magnetic nanofluid

Magnetic nanofluids used as the core liquid in the micro-electric transformer obtained by co-precipitation method [27, 35], is a colloidal suspension of nanoparticles of magnetite (Fe₃O₄), covered with a layer of surfactant oleic acid and dispersed in transformer oil. The main steps in

Processing option: all elements analyzed (normalized); all results in weight%										
Spectrum	In stats.	C	O	Al	Si	Ca	Mn	Fe	Zn	Total %
Spectrum 1	Yes	32.45	27.82	–	0.17		6.99	26.69	5.88	100.00
Spectrum 2	Yes	55.59	21.24	1.18	3.78	2.13	2.92	11.22	1.95	100.00
Spectrum 3	Yes	31.73	28.83	–	0.39	–	6.50	26.67	5.87	100.00
Spectrum 4	Yes	36.77	25.41	–	0.60	–	6.53	25.41	5.28	100.00
Spectrum 5	Yes	33.90	29.16	–	0.60	–	6.19	24.83	5.32	100.00
Spectrum 6	Yes	54.25	10.65	0.16	0.63	0.53	6.15	23.36	4.27	100.00
Spectrum 7	Yes	20.86	28.69	–	0.28	–	8.87	34.09	7.21	100.00
Max.		55.59	29.16	1.18	3.78	2.13	8.87	34.09	7.21	
Min.		20.86	10.65	0.16	0.17	0.53	2.92	11.22	1.95	

Table 2. Normalized values of elements obtained from spectral analysis of ferrite 3F3, corresponding to Spectrum 1–7, 2000× magnification.

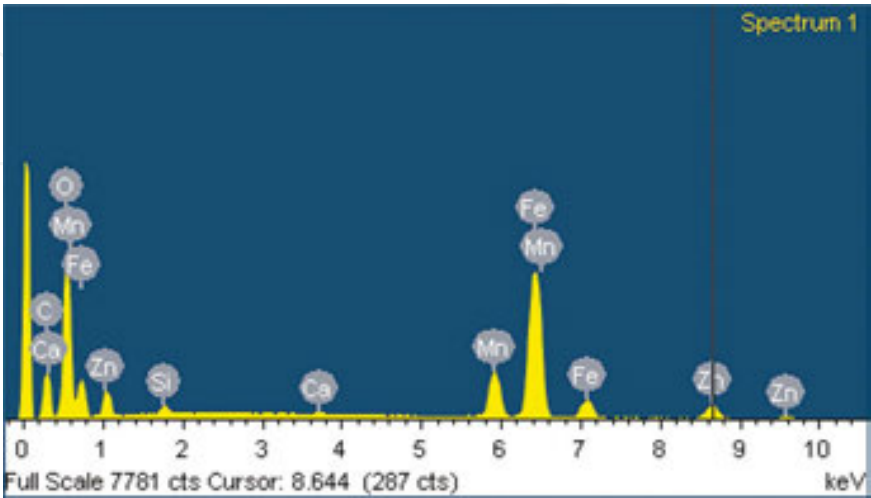


Figure 30. The 3F3 spectra analyze, corresponding to Spectrum 1 and 2000× magnification.

the synthesis procedure for obtaining magnetic nanofluids based on non-polar organic liquids are indicated in [28–30, 35]. To be used as a transformer fluid core, magnetic nanofluid requires good colloidal stability and features adapted to the operating conditions and materials it is in contact with. The magnetic feature is the most important for this application that requires a high saturation magnetization, **Figure 31**.

The maximum volume fraction was set around 23% and the recommended saturation magnetization values ranging between 500 Gs and 1000 Gs. The quality of magnetic nanofluids (NFM) is related to many details of the synthesis process and their stabilization/dispersion in the base fluid (in our case the UTR40 transformer oil). Among these we mention the coprecipitation temperature, Fe^{2+} molar ratio to Fe^{3+} , agitation rate, chemisorption temperature, reaction time, and so on. An essential aspect is the complete coverage of NFM with stabilizer and the elimination of the primary non-adsorbed primary surfactant. Repeated flocculation/redispersing NFM's remain coated with the optimal amount of surfactant [34, 35].

3.2.2. Making a miniature planar microtransformers with circular spiral windings with hybrid core—ferrite and colloidal magnetic nanofluid: V3

Planar microtransformers with circular spiral windings with hybrid core—ferrite and colloidal magnetic nanofluid is used in electronic circuits as a separator transformer in the DC/DC converter in harvesting energy applications. The use of a specific colloidal magnetic nanofluid with high saturation magnetization between 500 Gs and 1000 Gs, as a liquid core as part of the magnetic circuit eliminates all air gaps and also the magnetic field of dispersion. Achieving an improved magnetic coupling is obtained by constructive form of planar coils. Use of symmetrically overlaid ferrite cores, **Figure 32**, in conjunction with the magnetic nanofluid to the magnetic circuit assembly, determines the extension of the frequency range up to 1000 Mhz, **Figure 38**. This planar microtransformer, **Figures 32 and 36**, is made up of a planar coils assembly, a magnetic circuit assembly and a housing assembly. Regarding the planar coils, these respect the same manufacturing technology (**Figure 33 and 34**).

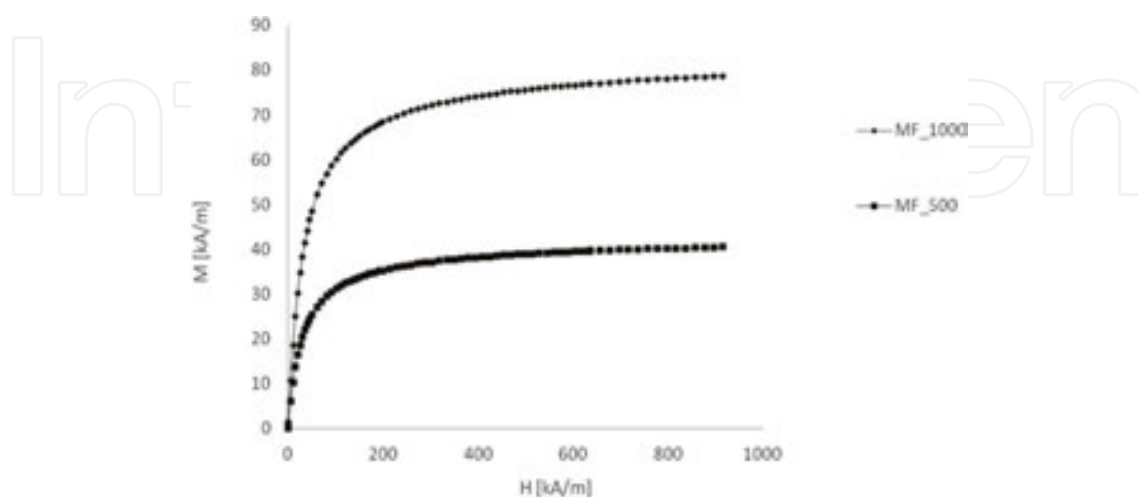


Figure 31. The first magnetization curve for analyzed NMF-UTR40-1000G and NMF-UTR40-500G samples (NMF-UTR40-1000G with $M_s = 78.61$ kA/m and NMF-UTR40-500G with $M_s = 40.51$ kA/m) [34].

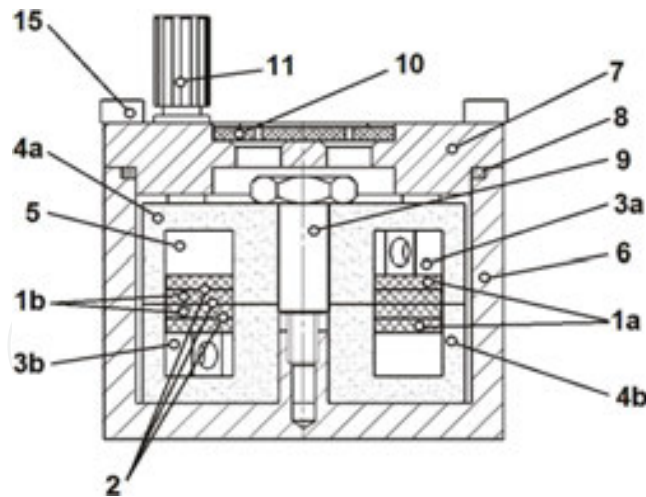


Figure 32. The section through a planar microtransformer with circular spiral windings **1a** and **1b**, with hybrid core—ferrite **4a** and **4b** and colloidal magnetic nanofluid **5**.

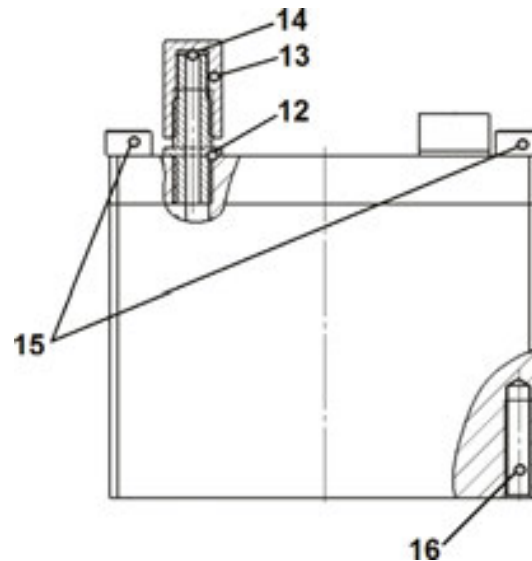


Figure 33. The section through a casing assembly.

A. The planar coils assembly

The planar coils assembly consists of four planar coils, **Figures 32** and **34a** and **Figure 34c**, respectively two identical planar coils, **1a** and two identical planar coils **1b**, each disposed on a glass-textolite plate of 1 mm thickness and diameter in the range 35–45 mm, covered on both sides with a copper layer thickness 35 μm and made by milling with a gap between 0.2–0.5 mm, dimensioned according to the current flow through the planar coils. Each primary planar coil, **1a**, is formed of two semi-windings connected in series, double-sided disposed on the same glass-textolite plate. The two semi-windings each have 20 turns made by milling on the glass-textolite plate. Then the two semi-windings are inserted between them resulting in a primary coil **1a**. Each secondary planar coil, **Figures 34a** and **34c**, **1b**, is formed of two semi-windings connected in series, double-sided disposed on the same glass-textolite plate. Also,

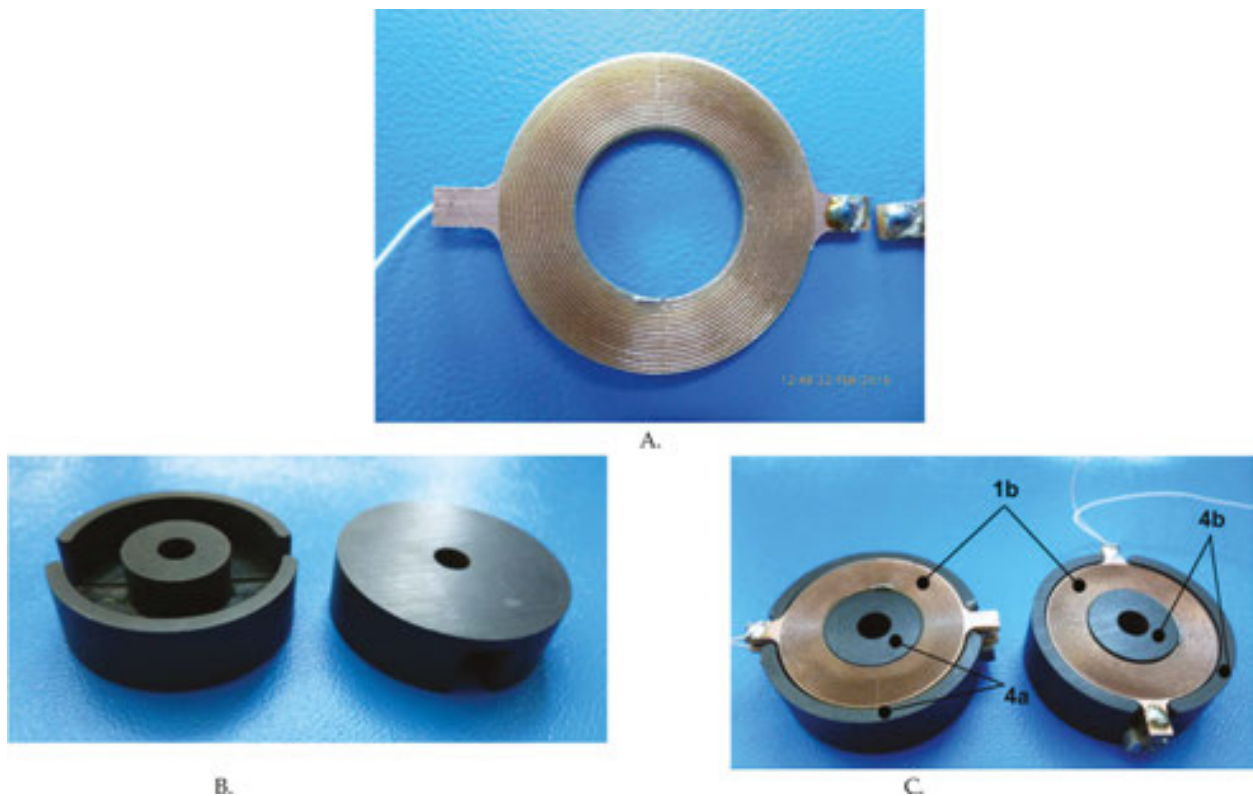


Figure 34. (a) Planar coil, (b) magnetic ferrite cores and (c) arrangement of planar coils in ferrite cores, practical achievements.

the two semi-windings each have 20 turns made by milling on the glass-textolite plate. Then the two semi-windings are inserted between them resulting in a secondary coil **1b**. All coils are isolated from each other by three insulation, **2**, of 0.1 mm thick made of “hostaphan” (polyethylene terephthalate), **Figure 12**. The planar coils assembly are fixed relative to the two upper **4a** and lower **4b** magnetic cores by means of two spacers **3a** and **3b** made of glass-textolite, **Figure 32**.

B. The magnetic circuit assembly

The magnetic circuit assembly consists of: two magnetic cores, top **4a** and bottom **4b**, 3F3 of the „pot” type, identical from ferrite, symmetrically overlapping according to **Figures 32** and **34b**; a liquid core consisting of a magnetic nanofluid, **5**, **Figure 32** in which are immersed the planar coil assembly and the two magnetic cores **4a** and **4b** **Figure 34 C**, placed in the casing assembly. The role of a liquid core made of a magnetic nanofluid as part of the magnetic circuit, eliminates all air gaps and also the magnetic field of dispersion. The most important magnetic feature for this usage is high saturation magnetization, between 500 Gs and 1000 Gs, **Figure 31**. Volume fraction (the ratio between the volume of magnetite nanoparticles and the volume of the entire magnetic nanofluid) corresponding to this saturation magnetization is in the range of 22–24%.

C. The casing assembly

The casing assembly, **Figure 35**, in which are immersed in magnetic nanofluid both the planar coils assembly and the magnetic circuit assembly. **Figure 36** shows a planar microtransformer



Figure 35. Parts of the casing assembly.



Figure 36. The planar microtransformer with circular spiral windings with hybrid core—ferrite and colloidal magnetic nanofluid, practical achievements.

with circular spiral windings with hybrid core—ferrite and colloidal magnetic nanofluid, practical achievements. The casing assembly, **Figures 32 and 33** consists of the box **6** and the lid **7**, both made by duralumin, the gasket **8** and the central screw **9**, which is fixing the magnetic circuit and the planar coils with the box **6**. The lid **7** contains the plate with terminals **10**, the system of the magnetic nanofluid supply **11** (made by a supply nozzle **12**, by a nozzle lid **13** and a nozzle gasket **14**), fixing screws **15** and four location screws **16**.

As I have shown, by using a specific magnetic nanofluid with high saturation magnetization, ranging between 500 Gs and 1000 Gs, as a liquid core of a magnetic circuit, the air gaps and the dispersive magnetic field lines are removed. Thus, magnetic nanofluid is used both as a coolant and as part of the hybrid magnetic core. Also, an improved magnetic coupling by up to 10% is noticed, together with an increase of the overall efficiency by up to 5%. As we will see below, experimental measurements in dynamic mode proves extension of the frequency range up to 1000 MHz, by symmetrical superposition of the ferrite magnetic cores in conjunction with the specific magnetic nanofluid.

3.2.2.1. Experimental measurements on the planar microtransformer with circular spiral windings with hybrid core—ferrite and colloidal magnetic nanofluid

A. Experimental measurements performed in static mode

Static mode measurements have been made with the bridge “Precision LCR Agilent E 4980A” for the microtransformer without magnetic nanofluid as well as for the microtransformer with hybrid core—ferrite and colloidal magnetic nanofluid with 500 Gs saturation magnetization, for a frequency variation in the range of 100–300 kHz (**Figure 36**).

Number of turns of the primary coil are $N_1 = 80$ turns and number of turns of the secondary coil are $N_2 = 80$ turns, (separator transformer). The bridge “Precision LCR Agilent E 4980A” it is used with option LEVEL = 2 V.

Analyzing the results obtained, synthesized in **Tables 3** and **4**, following conclusions are resulted:

- in the presence of magnetic nanofluid, the quality factor for the primary planar coil as well as the quality factor for the secondary planar coil increases significantly;
- there is a better frequency behavior in the presence of magnetic nanofluid.
- Experimental measurements performed on dynamic mode

In order to perform experimental measurements in dynamic mode, the transformer is connected in an electronic circuit diagram as shown in **Figure 37**. The Arbitrary Waveform Generator FLUKE PM 5138A was set to provide an excitation signal with a rectangular

Measured parameters for primary coil in the case if not magnetic nanofluid

Frequency	100 kHz	150 kHz	200 kHz	250 kHz	300 kHz
L_{p1} [mH]	3.672	2.129	1.378	0.981	0.75
D_1 [–]	4.45	3.743	3.117	2.647	2.3
Q_1 [–]	0.23	0.27	0.32	0.38	0.44
G_1 [mS]	1.92	1.865	1.793	1.712	1.624
R_{p1} [Ω]	520	536.32	557.58	584.25	615.78
R_{dc1} [Ω]	10.64	10.64	10.64	10.64	10.64

Measured parameters for secondary coil in the case if not magnetic nanofluid

L_{p2} [mH]	2.89	1.615	1.051	0.764	0.600
D_2 [–]	3.292	2.6	2.091	1.739	1.488
Q_2 [–]	0.3	0.38	0.48	0.57	0.67
G_2 [mS]	1.8	1.705	1.581	1.448	1.314
R_{p2} [Ω]	553.5	586.64	632.47	690.75	761
R_{dc2} [Ω]	10.8	10.8	10.8	10.8	10.8

Table 3. Measured parameters for primary and secondary coil in the case if not magnetic nanofluid.

Measured parameters for primary coil in the case with presence of magnetic nanofluid					
Frequency	100 kHz	150 kHz	200 kHz	250 kHz	300 kHz
L_{p1} [mH]	3.23	1.725	1.1	0.79	0.614
D_1 [–]	4.34	3.30	2.64	2.21	1.92
Q_1 [–]	0.23	0.3	0.38	0.45	0.52
G_1 [mS]	2.13	2.03	1.91	1.78	1.65
R_{p1} [Ω]	470	492	522	560	602
R_{dc1} [Ω]	10.62	10.62	10.62	10.62	10.62
Measured parameters for secondary coil in the case with presence of magnetic nanofluid					
L_{p2} [mH]	1.9	1.09	0.782	0.635	0.555
D_2 [–]	2.143	1.54	1.22	1.024	0.89
Q_2 [–]	0.46	0.64	0.81	0.97	1.11
G_2 [mS]	1.788	1.5	1.246	1.029	0.859
R_{p2} [Ω]	559	664	802.54	971	1160
R_{dc2} [Ω]	10.8	10.8	10.8	10.8	10.8

Table 4. Measured parameters for primary and secondary coil in the case with presence of the magnetic nanofluid, NMF-UTR40-500G type.

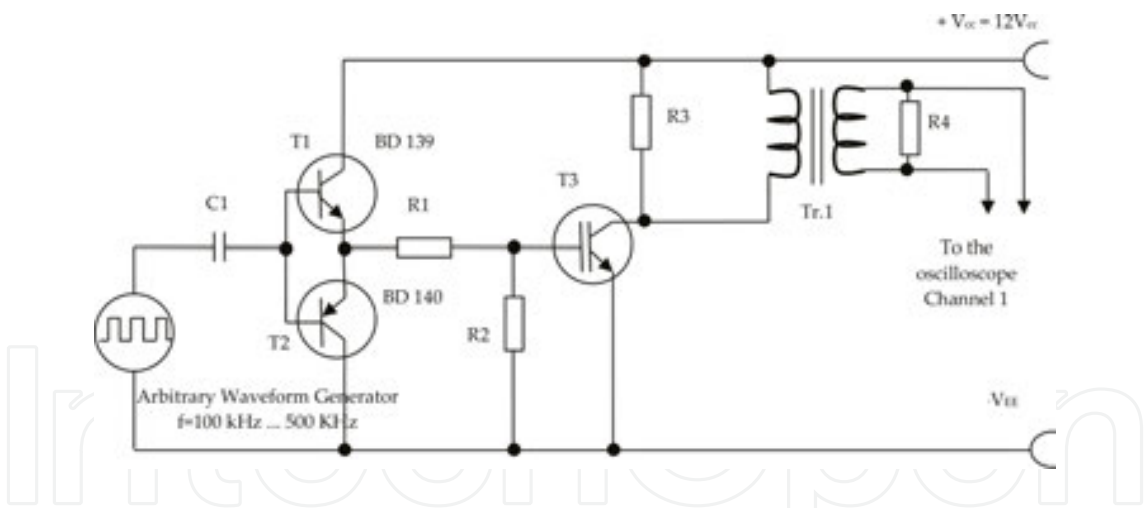


Figure 37. Electronic circuit diagram for testing the planar microtransformer with circular spiral windings with hybrid core—ferrite and colloidal magnetic nanofluid, on dynamic mode.

waveform, with features: the amplitude 10 V peak-to-peak, duty cycle $k = 50\%$ and frequency in the range of $f = 100$ to 1000 kHz. In Blue, at the bottom, **Figure 18**, the waveform capture of the arbitrary function generator is highlighted. Also, the output (secondary winding) waveforms capture in yellow, at the top is highlighted, **Figure 38**. Both waveforms captures are achieved with a digital oscilloscope Tektronix TDS 2014B.

The waveforms capture results for the frequency in the range of $f = 100$ to 1000 kHz can be concluded as shown in **Figure 38a–h**. These shows a good behavior of the planar microtransformer

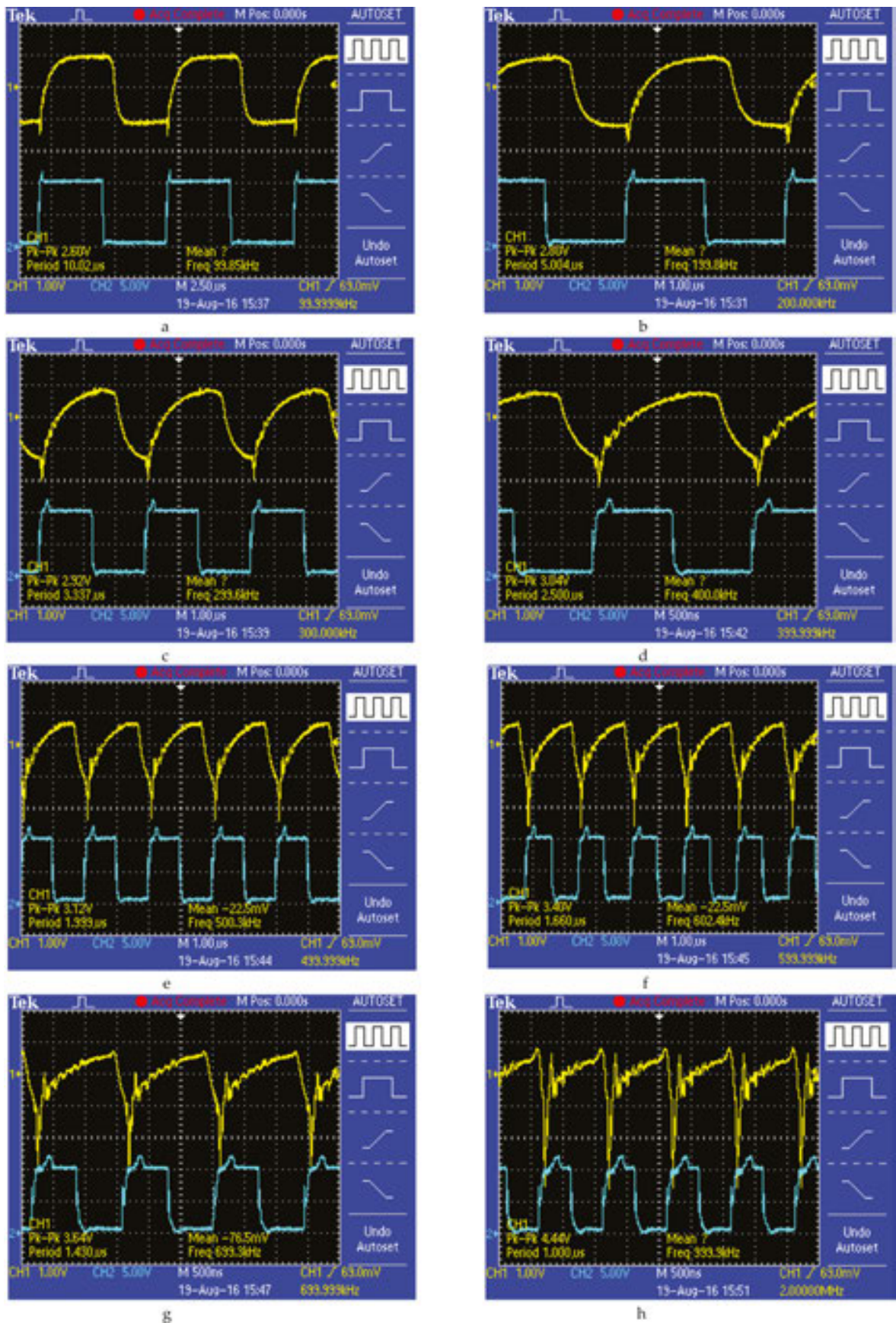


Figure 38. The waveform capture of the arbitrary function generator at the bottom and the output (secondary winding) waveforms capture at the top is highlighted, for the frequency in the range of $f = 100\text{--}1000$ kHz, from a. to h.

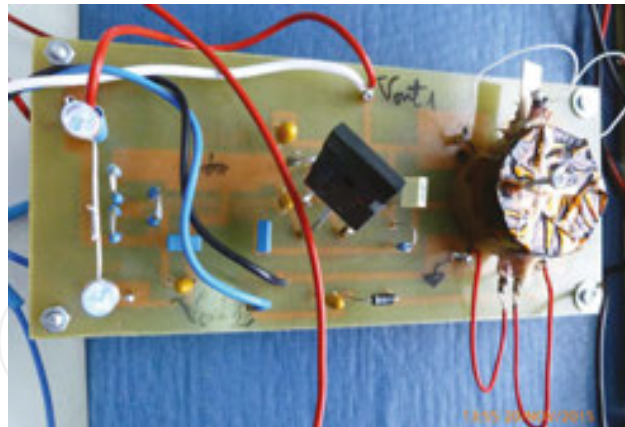


Figure 39. DC/DC converters, practical achievements for applications such as energy harvesting, made with the planar microtransformer with circular spiral windings with hybrid core—ferrite and colloidal magnetic nanofluid –V2.

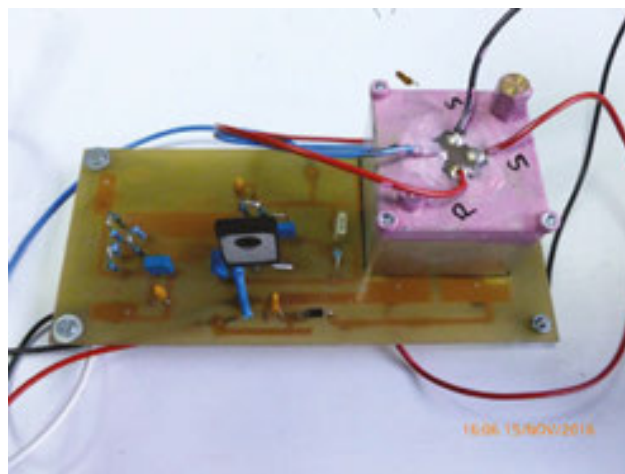


Figure 40. DC/DC converters, practical achievements for applications such as energy harvesting made with the planar microtransformer with circular spiral windings with hybrid core—ferrite and colloidal magnetic nanofluid –V3.

with circular spiral windings with hybrid core—ferrite and colloidal magnetic nanofluid. Thereby, it results in the possibility of using this type of transformer in DC/DC converters, for applications such as energy harvesting.

As shown in **Figures 39** and **40**, the planar microtransformer with circular spiral windings with hybrid core—ferrite and colloidal magnetic nanofluid –V2 and V3 is used in applications of energy harvesting. **Figure 41**, the electronic circuit diagram of DC/DC converter, designed for energy harvesting applications is shown.

3.2.3. Numerical simulation of the planar transformer with circular spiral windings with hybrid core-Ferrite and colloidal magnetic nanofluid-V4

3.2.3.1. CAD design

Variant V4 of the planar transformer corresponds to the DC/DC converters of high active power, that exceeding 100 watts. Choosing a particular type of magnetic nanofluid for a given application is an essential stage in design and can be facilitated by numerical modeling that

uses quantitative estimates of material properties (magnetoreological, thermal, magnetic, electrical, etc.) for the validation of numerical models used in designing and evaluating the behavior of the planar transformer. The evaluation of the magnetic flux inside the planar transformer with circular spiral windings with hybrid core—ferrite and colloidal magnetic nanofluid is done for two propose magnetic nanofluid, NMF-UTR40-50G and NMF-UTR40-500G, whose magnetization at saturation is of 50 Gs and 500 Gs respectively. Mathematical

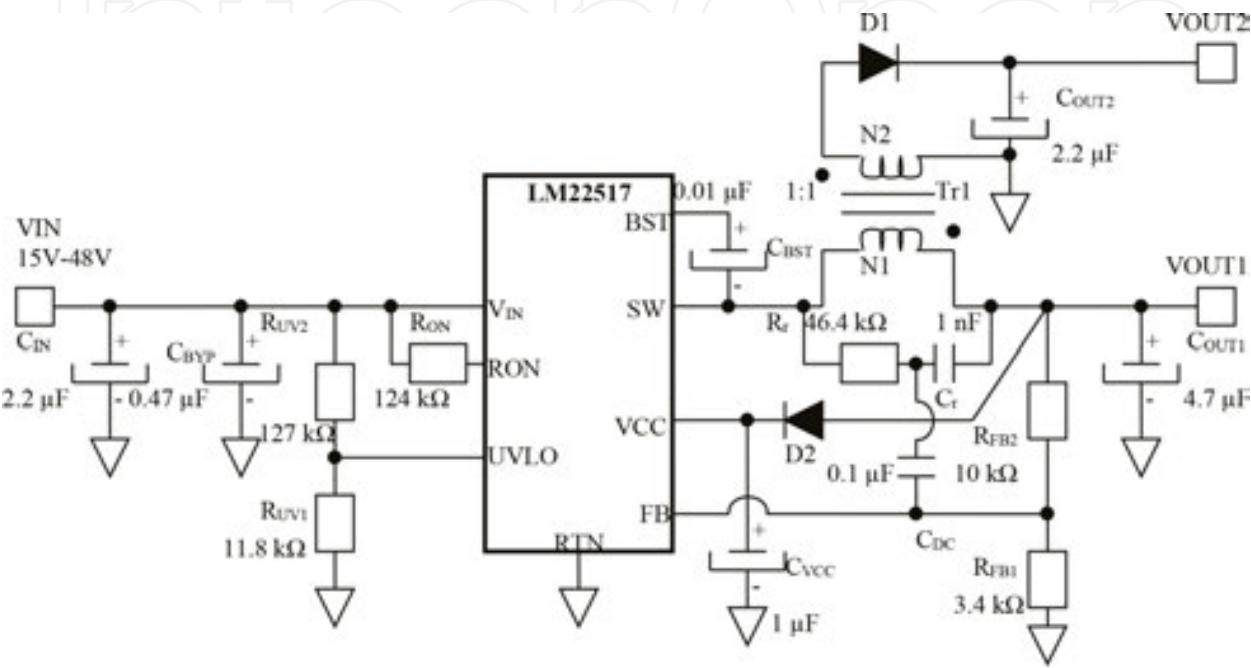


Figure 41. Electronic circuit diagram of DC/DC converter, designed for energy harvesting applications, made of LM22517 Texas Instruments and planar microtransformer with circular spiral windings with hybrid core—ferrite and colloidal magnetic nanofluid [33, 36, 37].

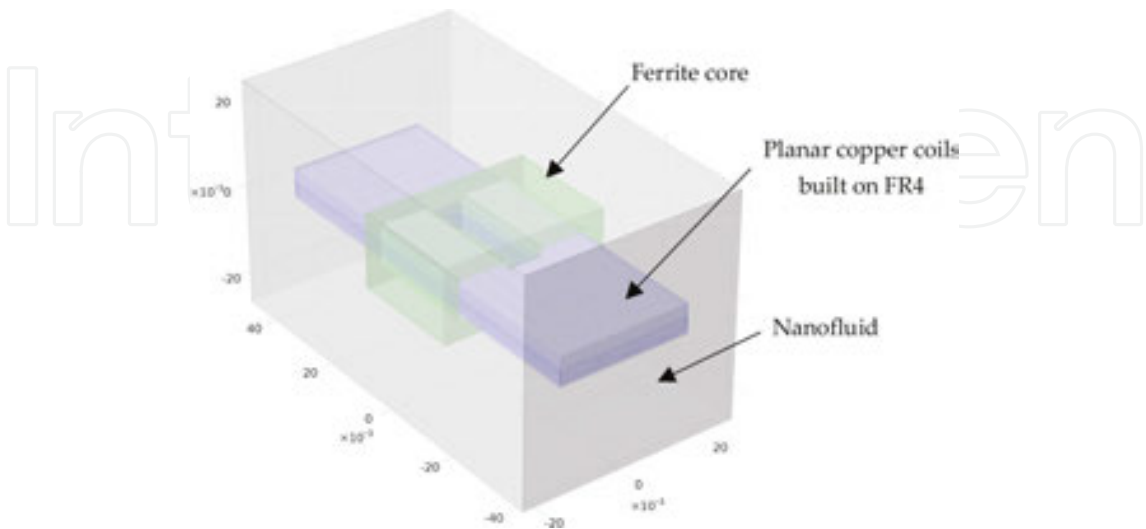


Figure 42. The CAD design and computational domain of the transformer submerged in magnetic nanofluid NMF-UTR40-50G or NMF-UTR40-500G.

models and numerical simulation are defined, under stationary hypothesis, by the finite element (FEM) technique [38, 39]. The computational domain was constructed by CAD methods, based on the design dimensions of the transformer, **Figure 42**.

Also, the details of the primary and secondary windings profiles are shows in **Figures 43** and **44**. To reduce the complexity of the model and the computational efforts, some elements (e.g. between layers, supports, etc.) have been excluded from the computational domain.

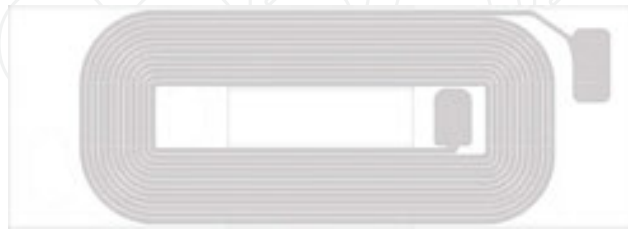


Figure 43. Details of the primary windings profiles.

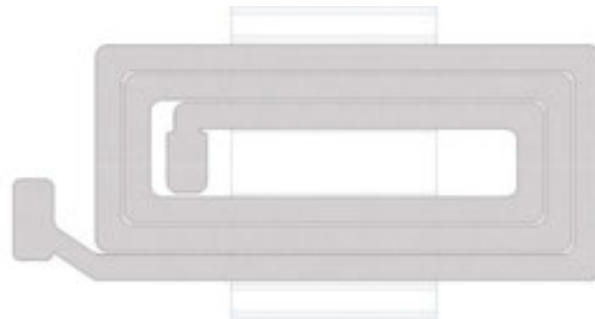


Figure 44. Details of the secondary winding profiles.

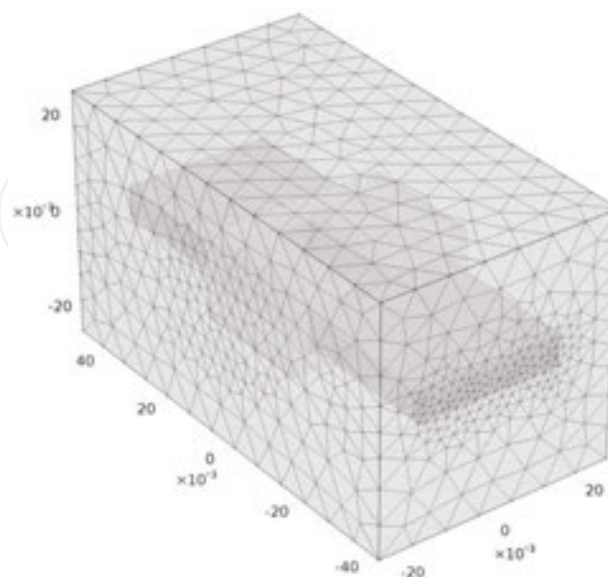


Figure 45. The discretization network (mesh) of the transformer, numerical model.

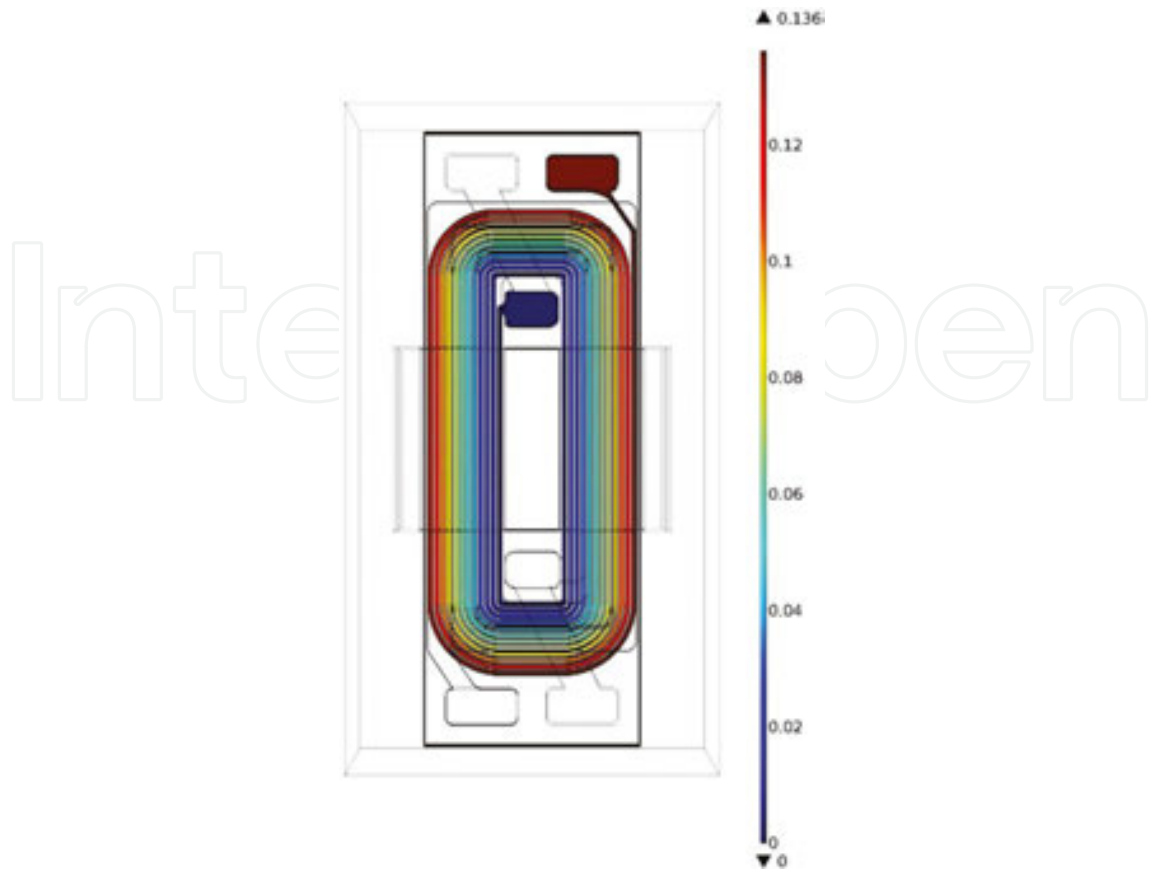


Figure 46. The spectra of electric field in the primary planar copper winding by colored boundary map in volts.

The problem is solved by the Galerkin finite element (FEM) technique. A discretization network consisting of 850,000, tetrahedral, quadratic Lagrange elements was generated automatically to model the field, **Figure 45**.

3.2.3.2. Mathematical model

The magnetic field source, the electrical currents in the windings, must be known. Therefore, an electrokinetic field analysis is defined by the partial differential equation (PDE). Firstly, the magnetic field source as well as the electrical currents in the windings must be known. Therefore, an electrokinetic field analysis is defined by the partial differential equation, (14), (15), (16) and (17),

$$\nabla_t \cdot d(\sigma \nabla_t V) = dQ_j \quad (14)$$

where σ [S/m] is the electrical conductivity, Q_j [W/m³] is an external current source and d [m] is the thickness of the shell. The operator ∇_t represents the tangential derivative along the shell [40]. The stationary magnetic field is computed by solving [38–40],
for the copper windings and free space

$$\nabla \times (\mu_0^{-1} \mu_r^{-1} \nabla \times \mathbf{A}) = \mathbf{J}_s^e, \quad (15)$$

for the magnetic fluid

$$\nabla \times (\mu_0^{-1} \mu_r^{-1} \nabla \times \mathbf{A} - \mathbf{M}) = 0, \quad (16)$$

where \mathbf{A} [T·m] is the magnetic vector potential, \mathbf{J}_s^e [A/m²] is the external electric current density of the shell ($\mathbf{J}_s^e \neq 0$ inside the planar coils), $\mu_0 = 4\pi \times 10^{-7}$ [H/m] is the magnetic permeability of free space, and μ_r is the relative permeability. For the 3CP90 ferrite core $\mu_r = 1720$ and for the copper windings and the free space $\mu_r = 1$. Also, \mathbf{M} [A/m] is the magnetization in the magnetic nanofluid, approximated by the analytic formula [40],

$$M = \alpha \arctan(\beta H), \quad (17)$$

here H [A/m] is the magnetic field strength, and α, β are empiric constants selected to fit the experimental magnetization characteristic of the magnetic nanofluid ($\alpha = 3050$ A/m and $\beta = 1.5 \times 10^{-5}$ m/A for the NMF-UTR40-50G, respectively, $\alpha = 4.85 \times 10^4$ A/m and $\beta = 2.5 \times 10^{-5}$ m/A for NMF-UTR40-500G).

3.2.3.3. Numerical simulation results

An iterative flexible generalized minimum residual solver (FGREMS) was used to solve the mathematical model (5), (6), (7) and (8). **Figures 46** and **47** present the electric field in the windings by voltage boundary color map, boundary conditions were chosen for nominal working conditions of the transformer are considered.

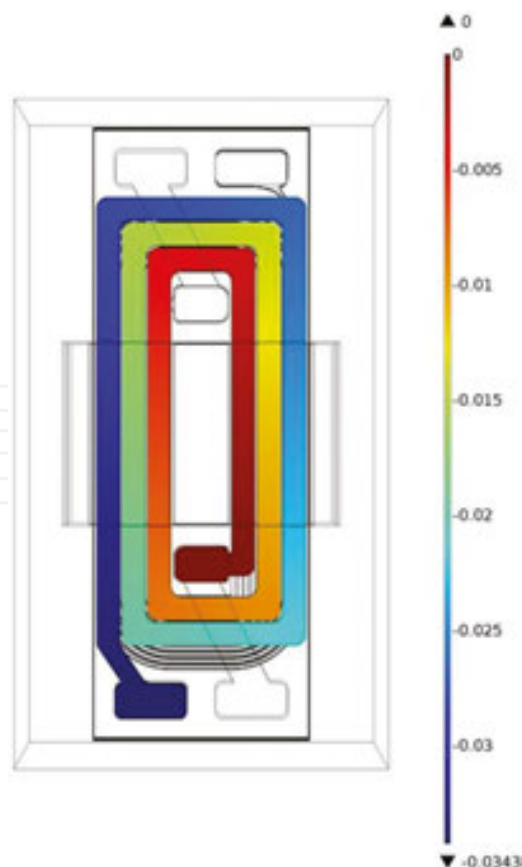


Figure 47. The spectra of electric field in the secondary planar copper winding by colored boundary map in volts.

The current shell density resulting from the electric field problem is used to solve the magnetic field problem in the transformer. **Figure 48** shows the magnetic field in the transformer submerged in the magnetic nanofluid NMF-UTR40-50G through field lines for different

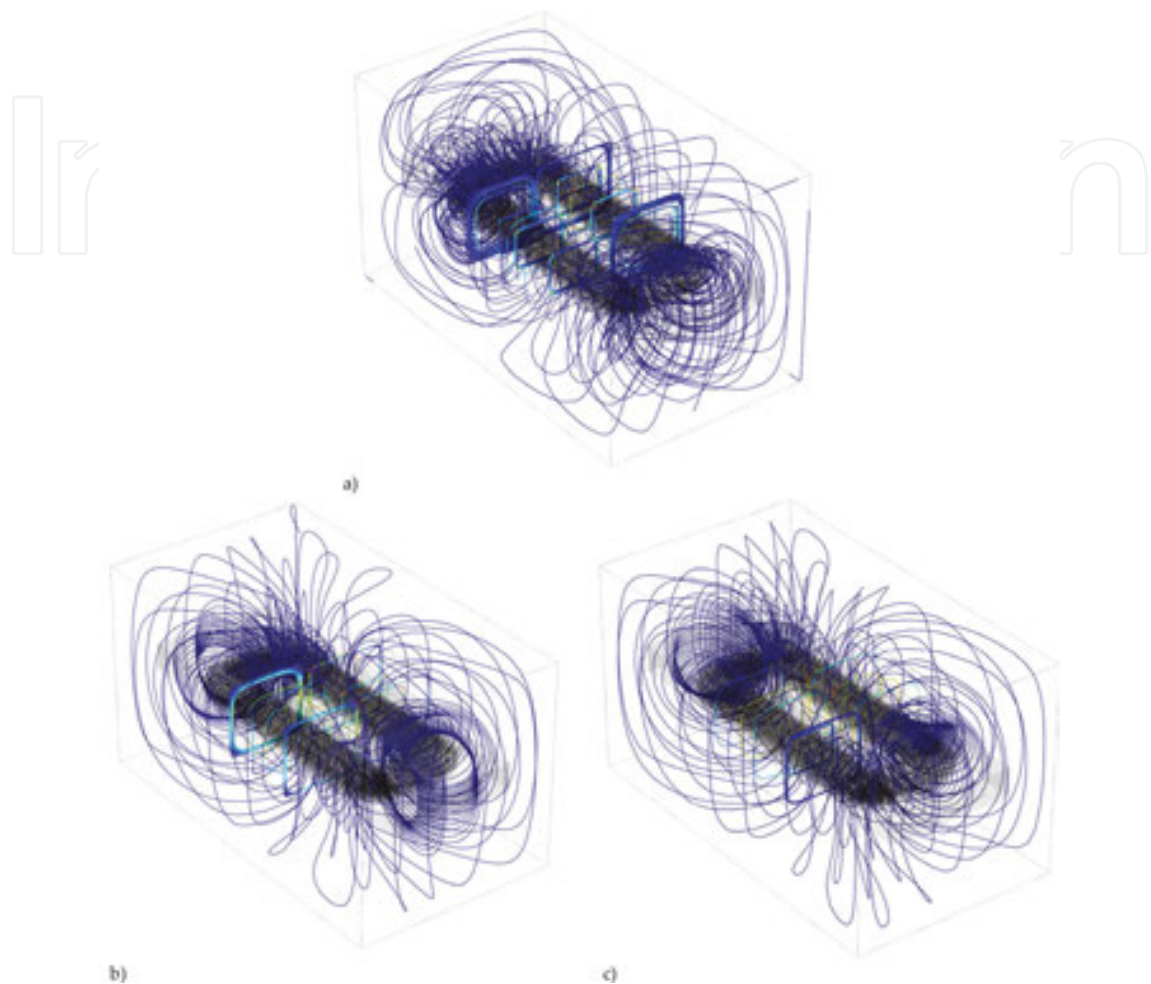


Figure 48. Magnetic flux density (tubes) for different powering schemes (NMF-UTR40-50G magnetic nanofluid).

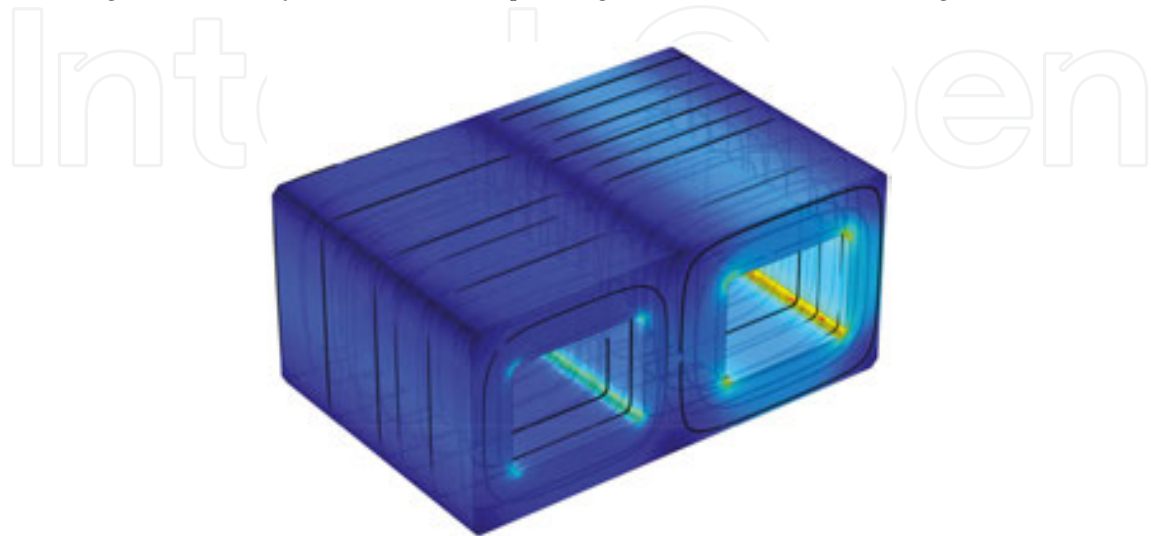


Figure 49. Normalized magnetic induction, by boundary color map, and tubes of magnetic flux density.

powering alternatives: (a) both windings are “ON”, the currents are in opposite directions – differential magnetic fluxes, (b) primary winding is “ON” and secondary winding is “OFF” and (c) primary winding is “OFF” and secondary winding is “ON”.

The magnetic field simulation result indicates that the fascicular magnetic field lines close mainly through the ferrite core, which offers a lower reluctance path than the magnetic nanofluid. In **Figure 49** the flux inside the solid ferrite core is presented by color map of normalized magnetic induction, B , as well as the lines of magnetic field density.

The magnetic field problem was solved also for the NMF-UTR40-500G magnetic nanofluid which has higher saturation limit, **Figure 50** shows the magnetic flux density (tubes) for different powering schemes.

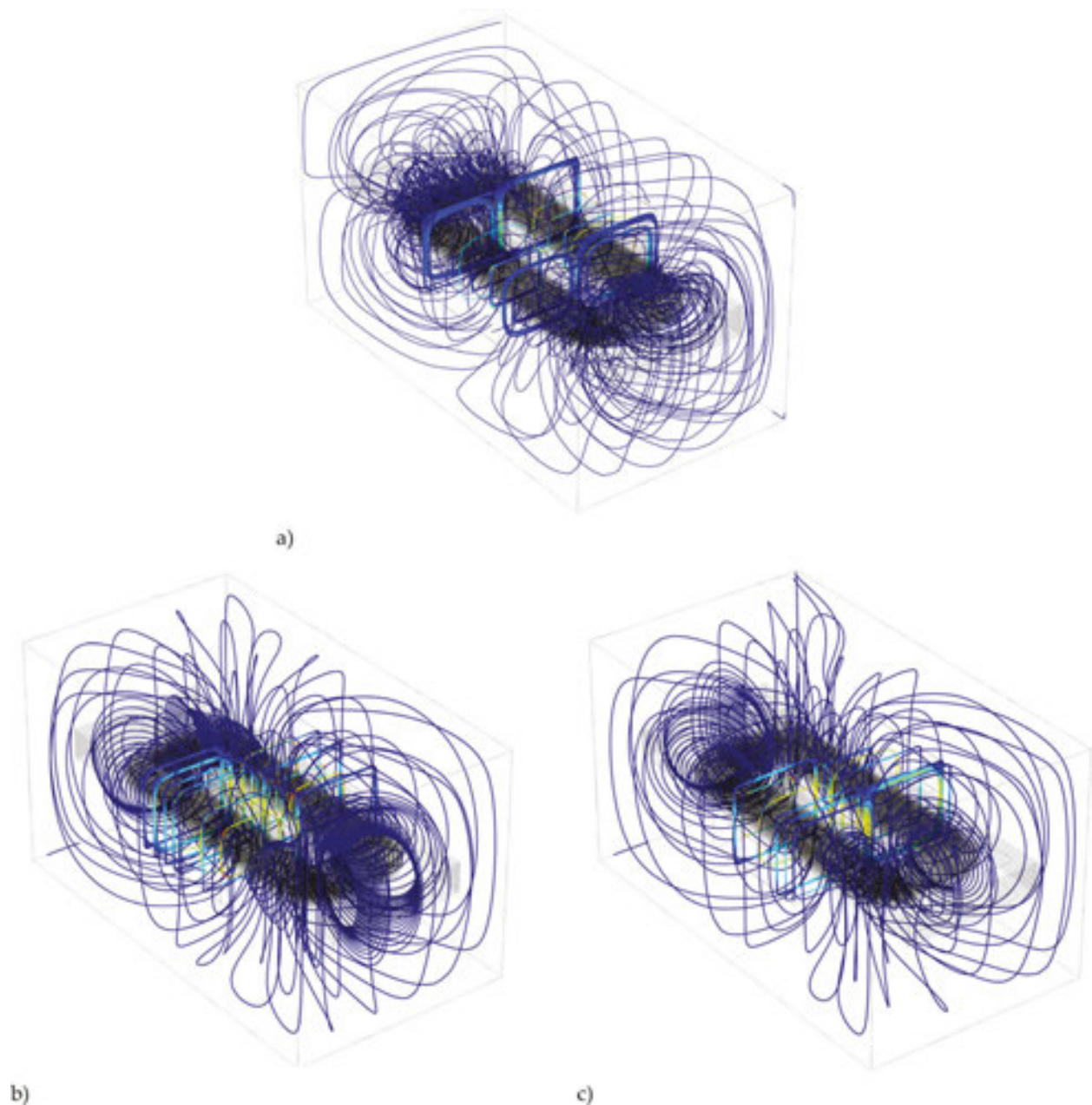


Figure 50. Magnetic flux density (tubes) for different powering schemes (NMF-UTR40-500G magnetic nanofluid).

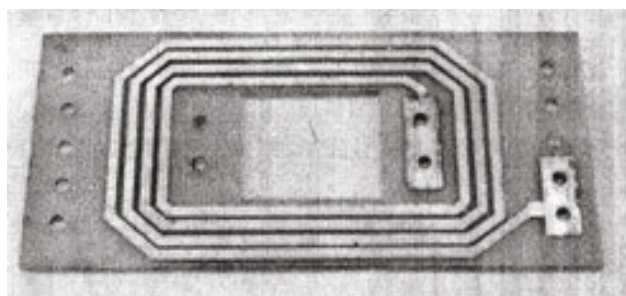


Figure 51. Planar coil corresponding to primary and secondary coils, practical achievements.

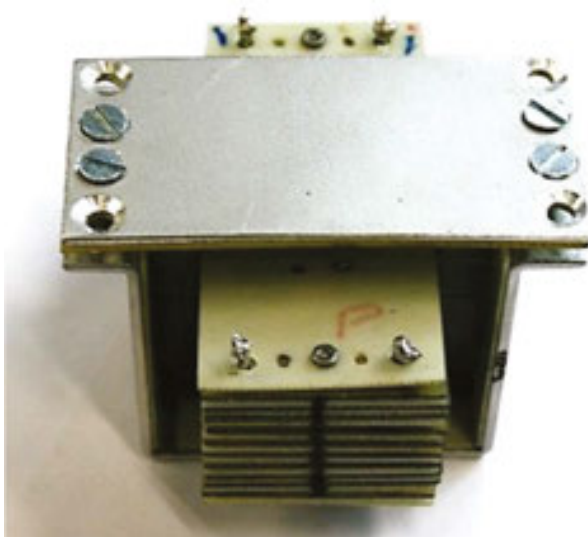


Figure 52. Planar transformer with planar windings with hybrid core—ferrite and colloidal magnetic nanofluid—V4, practical achievements.

The result indicates insignificant differences between the two types of magnetic nonfluids in terms of the magnetic flux distribution inside the fluid part of the magnetic core. However, because of the higher saturation limit, the NMF-UTR40-500G it is expected to perform better in higher power applications. For different models, the numerical investigations was performed under steady state conditions, to estimate the lumped parameters of the transformer and to evaluate the thermal behavior [41].

Figure 51 shows the planar coil corresponding to primary and secondary coils, practical achievements, for V4 variant of planar transformer. Also, **Figure 52** shows the practical achievement of the planar transformer with planar windings with hybrid core—ferrite and colloidal magnetic nanofluid — V4 variant.

Acknowledgements

The authors express special thanks to Dr. Jean Bogdan Dumitru, researcher at University Politehnica of Bucharest, Romania, for valuable results concerning the numerical simulations

and also to Dr. Elena Chitanu, researcher at National Institute for Electrical Engineering ICPE-CA, Bucharest, Romania, for valuable results concerning the development of technologies to obtain ZnO nanostructured materials. The research was performed with the support of UEFISCDI, PNCDI II Programme – Joint Applied Research Projects, Romania, Contract 63/2014, “Environment energy harvesting hybrid system by photovoltaic and piezoelectric conversion, DC/DC transformation with MEMS integration and adaptive storage”.

Nomenclature

- L_{p1} inductance of the primary coil, corresponding to an equivalent $L_{p1} - R_{p1}$ pattern disposed in parallel;
- L_{p2} inductance of the secondary coil, corresponding to an equivalent $L_{p2} - R_{p2}$ pattern disposed in parallel;
- D_1 tangent of the loss angle for the primary coil;
- D_2 tangent of the loss angle for the secondary coil;
- Q_1 Quality factor for the primary coil;
- Q_2 Quality factor for the secondary coil;
- G_1 conductivity ($1/R_{p1}$) of the primary coil, corresponding to an equivalent $L_{p1} - R_{p1}$ pattern disposed in parallel;
- G_2 conductivity ($1/R_{p2}$) of the secondary coil, corresponding to an equivalent $L_{p2} - R_{p2}$ pattern disposed in parallel;
- R_{p1} the resistance of the primary coil, corresponding to an equivalent $L_{p1} - R_{p1}$ pattern disposed in parallel;
- R_{p2} the resistance of the secondary coil, corresponding to an equivalent $L_{p2} - R_{p2}$ pattern disposed in parallel;
- R_{dc1} the resistance of the primary coil measured in DC;
- R_{dc2} the resistance of the secondary coil measured in DC.

Author details

Lucian Pîslaru-Dănescu^{1*} and Lipan Laurențiu Constantin²

*Address all correspondence to: lucian.pislaru@icpe-ca.ro

1 National Institute for Electrical Engineering ICPE-CA, Bucharest, Romania

2 University Politehnica of Bucharest, Bucharest, Romania

References

- [1] Pan ZW, Dai ZR, Wang ZL. Nanobelts of semiconducting oxides. *Science*. 2001;**291**(5510): 1947-1949
- [2] Levin A, Davydov B, Nikoobakht N. Growth habits and defects in ZnO nanowires grown on GaN/sapphire substrates. *Applied Physics Letter*. 2005;**87**:103110
- [3] Reiser A, Ladenburger GM, Prinz M, Schirra M, Feneberg L, Enchelmaier R, Li Y, Sauer R, Thonke K. Controlled catalytic growth and characterization of zinc oxide nanopillars on a-plane sapphire. *Journal of Applied Physics*. 2007;**101**:054319
- [4] Baxter J, Aydil ES, Cryst J. Epitaxial growth of ZnO nanowires on a- and c- plane sapphire. *Growth*. 2005;**274**:407-411
- [5] Lee W, Jeong MC, Myoung JM. Catalyst-free growth of ZnO nanowires by metal-organic chemical vapour deposition (MOCVD) and thermal evaporation. *Acta Materials*. 2004;**52**:3949-3957
- [6] Bai SN, Tsai HH, Tseng TY. Structural and optical properties of Al-doped ZnO nanowires synthesized by hydrothermal method. *Thin Solid Films*. 2007;**516**:155-158
- [7] Sun Y, Angwafor NGN, Riley DJ, Ashfold MNR. Synthesis and photoluminescence of ultra-thin ZnO nanowire/nanotube arrays formed by hydrothermal growth. *Chemical Physics Letter*. 2006;**431**:352-357
- [8] Park WI, Yi G, Kim M, Pennycock SL. ZnO nanoneedles non-catalytic vapor-phase epitaxy. *Advanced Materials*. 2002;**14**(24):1841-1843
- [9] Wu JJ, Liu SC. Low-temperature growth of well-aligned ZnO nanorods by chemical vapor deposition. *Advanced Materials*. 2002;**14**:215-218
- [10] Yang P, Yan H, Mao S, Russo R, Johnson J, Saykally R, Morris N, Pham J, He R, Choi HJ. Controlled growth of ZnO nanowires and their optical properties. *Advanced Functional Materials*. 2002;**12**(5):323-331
- [11] Yao BD, Chan YF, Wang N. Formation of ZnO nanostructures by a simple way of thermal evaporation. *Applied Physics Letters*. 2002;**81**:757-759
- [12] Sun Y, Fuge GM, Ashfold MNR. Growth of aligned ZnO nanorod arrays by catalyst-free pulsed laser deposition methods. *Chemical Physics Letters*. 2004;**396**:21-26
- [13] Huang MH, Mao S, Feick H, Yan H, Wu Y, Kind H, Weber E, Russo R, Yang P. Room-temperature ultraviolet nanowire nanolasers. *Science*. 2001;**292**:1897-1899
- [14] Yan HQ et al. ZnO nanoribbon microcavity lasers. *Advances Materials*. 2003;**15**:1907-1911
- [15] Green LE. Teza Master Next Generation Photovoltaics Using Solution Grown Zinc Oxide Nanowires Arrays. Berkeley: University of California; 2007. p. 10
- [16] Tsai FS, Wang SJ, Tu YC, Hsu YW, Kuo CY, Lin ZS, Ko RM. Preparation of p-SnO/n-ZnO heterojunction nanowire arrays and their optoelectronic characteristics under UV illumination. *Applied Physics Express*. 2011;**4**:025002

- [17] Bai SN, Wu SC. Synthesis of ZnO nanowires by the hydrothermal method, using sol-gel prepared ZnO seed films. *Journal of Materials Science*. 2011;**22**:339-344
- [18] Chițanu E, Pîslaru-Dănescu L, El-Leathey LA, Marin D, Chihaiu RA, Băbuțanu CA, Marinescu V, Sbârcea BG. Improvement of Polycrystalline Solar Cells Operation Under Low Solar Radiation Conditions by Using ZnO Nanostructured Materials. In: *Proceeding of 10th international symposium ATEE 2017 – Advanced Topics in Electrical Engineering*; 23-25 March 2017; Bucharest. Romania. pp. 768-773, E-ISBN: 978-1-5090-5160-1, USB ISBN: 978-1-5090-5159-5, Print on Demand (PoD) ISBN: 978-1-5090-5161-8 INSPEC Accession number: 16824692, DOI: 10.1109/ATEE.2017.7905074
- [19] Meulenkamp EA. Synthesis and growth of ZnO nanoparticles. *The Journal of Physical Chemistry. B*. 1998;**102**:5566-5572
- [20] Sakohara S, Ishida M, Anderson MAJ. Visible luminescence and surface properties of nanosized ZnO colloids prepared by hydrolyzing zinc acetate. *Physical Chemistry B*. 1998;**102**:10169-10175
- [21] McBride RA, Kelly JM, McCormack DEJ. Growth of well-defined ZnO microparticles by hydroxide ion hydrolysis of zinc salts. *Materials Chemistry*. 2003;**13**:1196-1201
- [22] Lin CC, Li YY. Synthesis of ZnO nanowires by thermal decomposition of zinc acetate dehydrate. *Materials Chemistry and Physics*. 2009;**113**:334
- [23] Sun Y, Fuge GM, Ashfold MNR. Growth of aligned ZnO nanorod arrays by catalyst-free pulsed laser deposition methods. *Chemical Physics Letters*. 2004;**396**:21-26
- [24] Huang MH, Mao S, Feick H, Yan H, Wu Y, Kind H, Weber E, Russo R, Yang P. Room-temperature ultraviolet nanowire nanolasers. *Science*. 2001;**292**:1897-1899
- [25] Pîslaru-Dănescu L, Morega M, Dumitru AI, Pintea J. Analysis of Piezoelectric Structures Based on New Modified PZT Zirconate Titanate Designed for Energy Harvesting Applications. In: *Proceeding of 10th international symposium ATEE 2017 – Advanced Topics in Electrical Engineering*; 23-25 March 2017; Bucharest. Romania. pp. 842-847, E-ISBN: 978-1-5090-5160-1, USB ISBN: 978-1-5090-5159-5, Print on Demand (PoD) ISBN: 978-1-5090-5161-8, DOI: 10.1109/ATEE.2017.7905075, (indexed on: IEEE Xplore, SCOPUS)
- [26] Lucian Pîslaru-Dănescu, Laurențiu Constantin Lipan, Ioana Pisciă, Ion Daniel Ilina, Alina Dumitru. New energy harvesting systems, designed for new piezoelectric transducers, with charging energy management. In: *International Conference and Exposition on Electrical and Power Engineering EPE 2014*; 16-18 October 2014; Iasi, Romania. In: *Proceedings of the International Conference and Exposition on Electrical and Power Engineering (EPE 2014)*; pp. 646-651. ISBN: 978-1-4799-5849-8, DOI: 10.1109/ICEPE.2014.6969989, Accession number: WOS:000353565300119, (indexed on: ISI WEB OF SCIENCE, IEEE Xplore, SCOPUS)
- [27] Morega AM, Dumitru JB, Morega M, Pîslaru-Dănescu L. Flow patterns in the magnetic nanofluid core of a miniature planar spiral transformer. *Environmental Engineering and Management Journal*. 2013;**12**(6):171-1177. ISSN: 1582-9596, eISSN: 1843-3707, Accession number: WOS:000325632500009, (indexed on: ISI WEB OF SCIENCE, SCOPUS), ISI impact factor in 2013= 1.258

- [28] Pîslaru-Dănescu L, Morega AM, Morega M, Stoica V, Marinică OM, Nouras F, Păduraru N, Borbáth I, Borbáth T. Prototyping a ferrofluid-cooled transformer. *IEEE Transactions on Industry Applications*. 2013;**49**(3):1289-1298. ISSN: 0093-9994, DOI: 10.1109/TIA.2013.2252872. Accession number: WOS:000319152500033, (indexed on: ISI WEB OF SCIENCE, IEEE Xplore, SCOPUS), ISI impact factor in 2013= 2,046
- [29] Pîslaru-Dănescu L, Morega AM, Telipan G, Morega M, Dumitru JB, Marinescu V. Magnetic nanofluid applications in electrical engineering. *IEEE Transactions on Magnetics*. 2013;**49**(11):5489-5497. ISSN: 0018-9464, E-ISSN: 1941-0069, DOI: 10.1109/TMAG.2013.2271607. Accession number: WOS:000326246500015, (indexed on: ISI WEB OF SCIENCE, IEEE Xplore, SCOPUS), ISI impact factor in 2013=1.213
- [30] Dumitru JB. "Contributions to the Analysis and Development of Ambient Energy Harvesting Systems" [Doctoral thesis]. University Politehnica of Bucharest, Romania; 2013
- [31] Dumitru JB, Morega AM, Morega M. Nanofluid cored miniature electrical transformer with planar spiral windings. *International Conference on Optimization of Electrical and Electronic equipment OPTIM 2014*. In: *Proceedings of the International Conference on Optimization of Electrical and Electronic Equipment (OPTIM 2014)*; May 22-24 2014; Bran, Romania. pp. 11-16, ISBN: 978-1-4799-5183-3, DOI: 10.1109/OPTIM.2014.6851037, Accession number: WOS:000343551300002, (indexed on: ISI WEB OF SCIENCE, IEEE Xplore, SCOPUS)
- [32] Morega AM, Morega M, Dumitru JB, Pîslaru-Dănescu L, Stoica V. Magnetic and electric sizing of a miniature planar spiral transformer. *7th International Conference and Exposition on Electrical and Power Engineering EPE 2012*. In: *Proceedings of the 2012 7th International Conference and Exposition on Electrical and Power Engineering (EPE 2012)*; 25-27 October 2012; Iasi, Romania. pp. 654-659, Published: 2012, ISBN: 978-1-4673-1172-4, Print ISBN: 978-1-4673-1173-1, DOI: 10.1109/ICEPE.2012.6463572, Accession number: WOS:000324685300118, (indexed on: ISI WEB OF SCIENCE, IEEE Xplore, SCOPUS)
- [33] Pîslaru-Dănescu L, Chițanu E, Chihaiu RA, Marin D, El-Leathay LA, Marinescu V, Sbârcea BG, Băbuțanu CA. New harvesting system based on photovoltaic cells with antireflexive ZnO nanoparticles coatings and DC/DC isolation conversion. In: *Proceeding of 4th International Symposium EFEA 2016 – Environmental Friendly Energies and Applications*; 14-16 September 2016; Belgrade, Serbia. pp. 1-6, E-ISBN: 978-1-5090-0749-3, DOI: 10.1109/EFEA.2016.7748798, (indexed on: ISI WEB OF SCIENCE, IEEE Xplore, SCOPUS)
- [34] Pîslaru-Dănescu L, Marius P, Cristinel-Ioan I, Rares-Andrei C, Corina-Alice B, Sergiu N, Florentina B, Daniela S, Sorin H, Oana-Maria M, Alexandru-Mihail M, Morega M, Dumitru JB, Popa N-C. Planar transformer with magnetic nanofluid. Patent Application No. OSIM A/00713 from 07-10-2016, applicants: INCDIE ICPE-CA Bucharest and Politehnica University of Timisoara
- [35] Pîslaru-Dănescu L, Telipan G, Stoian F, Holotescu S, Marinică OM. Chapter "Nanofluid with colloidal magnetic Fe₃O₄ nanoparticles and its applications in electrical engineering", pp 163-198, "Nanofluid Heat and Mass Transfer in Engineering Problems", Mohsen Sheikholeslami, InTech Europe, Rijeka, 2017, ISBN 978-953-51-4922-4, 10.5772/65556

- [36] Texas Instruments. LM25017 48-V, 650-mA Constant on-Time Synchronous Buck Regulator. Data sheet, SNVS951D, December 2014
- [37] Texas Instruments. AN-2292, Designing an Isolated Buck (Fly-Buck) Converter. Application report, SNVA674C, December 2014
- [38] "COMSOL Multiphysics Users Guide," ver. 3.5a (2010), 4.2a (2011), 4.3 (2012), Multiphysics Modeling, Finite Element Method and Engineering Simulation Software © 1998-2015, COMSOL A.B. Sweden
- [39] Tsai TH, Kuo LS, Chen PH, Lee DS, Yang CT. Applications of ferro-nanofluid on a micro-transformer. *Sensors*. 2010;10:8161-8172
- [40] Dumitru JB, Morega AM, Morega M. Nanofluid cored miniature electrical transformer with planar spiral windings. International Conference on Optimization of Electrical and Electronic Equipment Optim 2014. In: Proceedings of the International Conference on Optimization of Electrical and Electronic Equipment (OPTIM 2014); MAY 22-24 2014; Bran, Romania. pp. 11-16. ISBN: 978-1-4799-5183-3, DOI: 10.1109/OPTIM.2014.6851037, Accession number: WOS:000343551300002, (indexed on: ISI WEB OF SCIENCE, IEEE Xplore, SCOPUS)
- [41] Dumitru JB, Morega AM, Morega M, Pîslaru-Dănescu L. Forced flow patterns in a miniature planar spiral transformer with ferrofluid core. *INCAS Bulletin*. 2015;7(4):85-94, (online) ISSN 2247-4528 <http://bulletin.incas.ro>, (print) ISSN 2066-8201, ISSN-L 2066-8201, DOI: 10.13111/2066-8201.2015.7.4.8, ICID: 1185745, (indexed on: Copernicus, SCOPUS)

